Doctoral Thesis

Circular Orbits of Particles around Compact Objects and Their Observability

コンパクト天体周辺での粒子の円軌道とその観測可能性

Keisuke Nakashi

Department of Physics, Graduate School of Science,
Rikkyo University

Abstract

Recent observational progress about strong gravitational fields heralds the arrival of an era where we can observe phenomena happening around a compact object in various ways such as electromagnetic wave and gravitational wave observations. To investigate the motion of test particles around a compact object is one of the most fundamental problems for revealing the nature of the gravitational field generated by a compact object and relates to predicting various phenomena occurring around compact objects.

In this thesis, we focus on circular orbits of test particles. The appearance of the circular orbits around black holes is different from the case of the Newtonian potential. For timelike geodesics, the unstable circular orbits appear near a black hole. Also, the circular orbits are formed even for null geodesics. It is known that these circular orbits around black holes relate to the strong gravitational phenomena, for example, a black hole shadow, an accretion disk, etc.

We study the effect of a second compact object on the circular orbits. In particular, we investigate how stable circular orbits around a main compact object appear by using the Majumudar–Papapetrou dihole spacetime, which consists of the two extremal Reissner–Nordström black holes. While the parameter range of the separation of the two black holes is divided due to the appearance of stable circular orbits, this division depends on its mass ratio. We show that the mass ratio range separates into four parts, and we find three critical values as the boundaries.

We also study the escape probability of a photon emitted from the circular orbit of a (near-)extremal Kerr black hole. The escape probability evaluated at the innermost stable circular orbit (ISCO) decreases monotonically as the black hole spin increases. In the extremal black hole case, even if the orbital radius of the light source is arbitrarily close to the ISCO radius, which coincides with the horizon radius, the escape probability remains a nonzero value. We also see that the distant observer can observe blueshift photons.

Acknowledgments

I would like to thank my supervisor, Tomohiro Harada, for his instructive comments and discussions on my works during the doctoral course. I have learned many things about not only physics but also knowledge as a researcher from him. I also thank my collaborators, T. Igata, M. Kimura, S. Kobayashi, Y. Koga, K. Ogasawara, H. Saida, and S. Ueda, for their fruitful discussions, comments, and suggestions. I am also grateful to the examiners H. Tanaka and S. Yamada, for their useful suggestions and comments. I am grateful to T. Kobayashi, Y. Nakayama, H. Tanaka, Y. Hatsuda, T. Hiramatsu, and all colleagues of the theoretical physics group in Rikkyo University, in particular, K. Kozai, who is the secretary of our group. Finally, I cannot express my massive appreciation enough to my parents Kayoko and Kenichi, and my uncle Takatoshi Suetsugu for their lot of supports and to the rest of my family. My works were supported in part by Rikkyo University Special Fund for Research.

Contents

Chapter 1

Introduction

General relativity is a theory of gravity proposed by Albert Einstein in 1915 [1, 2]. Nowadays, general relativity is widely accepted as the most straightforward and most beautiful theory of gravity that describes the dynamics of our Universe, the interaction between matter and gravity, and so on. Experiments and observations show that some effects that are not explained by Newtonian gravity, such as the perihelion shift of mercury, can be described by general relativity [3]. General relativity describes interactions between matter fields and gravity fields via the Einstein equation. Roughly, the Einstein equation means that if matter exists, it generates gravity fields.

A black hole is one of the solutions of the Einstein equation, where the non-linearity of gravity is most noticeable. Karl Schwarzschild discovered the first black hole solution so-called the Schwarzschild black hole [4]. It describes the gravitational field around a spherically symmetric non-rotating point mass source. After some decades of it, Roy Kerr provided the rotating black hole solution [5]. The properties of these black hole solutions themselves were studied well. It is known that there is a singularity at the core of these black holes, and it is covered by the event horizon.

Black holes are the most compact celestial objects, and they are believed to be very common in the universe. Indeed, the existence of black holes has been supported by a lot of observations. The first such observation is the quasar observation. A quasar is a celestial object that emits enormous energy from a very compact region, and it is thought that black holes are necessary to explain this

observation. Also, there is a supermassive black hole at the center of most large galaxies, which is thought to be the origin of high energy phenomena such as a black hole jet. Recent observational progress, such as the first direct detection of gravitational waves by LIGO/Virgo collaboration [6] and the first image of the shadow of M87 galactic center (M87*) [7–12], have made the existence of black holes more confident.

Because black holes are invisible themselves, when we want to obtain the properties of a black hole from a observation, we need to predict phenomena occurring around a black hole and observable quantities. Investigating particle motions in a black hole spacetime is one of the fundamental way of such predictions, and reflects the properties of a black hole, for example, the mass and the angular momentum. Indeed, the observations of S2 that is one of the stars orbiting around Sagittarius A* shows excellent agreement with the geodesic motion in the Schwarzschild spacetime. The mass of the supermassive black hole located at the center of our galaxy has been estimated from the observation of S2 as $4 \times 10^6 M_\odot$ (see, for example [13–16]).

Circular orbits of test particles are related to various phenomena that occur around a black hole. In a black hole spacetime, even a photon is deflected its orbit due to the strong gravity fields around a black hole. Furthermore, at a certain radius, a photon can take a circular orbit. It is well known that a circular photon orbit relates to the formation of a black hole shadow. For timelike particles, the strong gravitational field around a black hole limits the region where timelike particles can take stable circular orbits. It can be said that the strong gravitational field around a black hole causes this limitation because, in Newtonian gravity, a timelike particle can take a circular orbit at an arbitrary radius except for the origin. The sequence of stable circular orbits plays a key role in the context of the formation of a accretion disk and the gravitational waves from a binary black hole. There is a typical radius that timelike particles cannot take stable circular orbits inside it. The typical radius is known as the innermost stable circular orbit (ISCO). The ISCO also relates to astrophysical phenomena because it is identified as the inner edge of a standard accretion disk model [17] and a compact binary switches the stage of the evolution from the inspiral phase to the merging phase there [18, 19].

Recently the existence of binary black holes has been strongly supported by

direct observation of gravitational waves supports. The LIGO Scientific and Virgo collaborations have already detected gravitational waves from 10 binary black hole mergers and a binary neutron star merger in the first and second observing runs [20]. Furthermore, this year, the result of the First-half observing run were announced and 39 new gravitational wave events have been added [21]. These results indicate that binary black hole systems are quite common in the universe.

In realistic cases, there exist other objects or matter distributions around binary compact objects. In Newtonian gravity, there are Poincaré's three-body problem and the Kozai mechanism as traditional problems for revealing interactions between two gravitational sources and a third body. In the relativistic context, many works investigating the three body problem have been done so far, for example, the relativistic three body problem [22, 23], the resonance in a compound extreme mass ratio inspiral/massive black hole binary [24], and the gravitational wave emission induced by a third body [25–29], etc.

Actual binary black hole systems is dynamical systems so that one needs to use the numerical method to analyze the phenomena in such systems. For example, the study of the shadow of a binary black hole requires a fully nonlinear analysis of the numerical relativity [30]. On the other hand, a perturbative approach, which perturbatively takes into account the dynamics of a binary black hole, is also used to provide a qualitative understanding of the phenomenon. This approach is valid if a timescale of a target phenomenon is sufficiently shorter than the dynamical timescale of a binary black hole. In this approach, we need to consider a static system before introducing dynamic properties. To this end, we employ some stationary (or static) dihole spacetime as a toy model. There are some exact dihole spacetime solutions of the Einstein equation (or the Einstein–Maxwell equation) such as the Weyl spacetime [31], the Majumdar–Papapetrou spacetime [32–34], the double-Kerr spacetime [35], etc. Such stationary dihole spacetime can reproduce the specific features of phenomena around a binary black hole. For instance, the eyebrows structure of the binary black hole shadow also appears in the (quasi)static dihole spacetime [36–40].

The first aim of this thesis is to study the effect of a second compact object on the circular orbits of test particles. We expect that the circular orbits exhibit nontrivial appearance under the influence of a second compact object. For this purpose, we adopt the Majumdar–Papapetrou (MP) dihole spacetime, which consists

of two extremal Reissner–Nordström black holes. In some previous works, several properties of circular orbits in the MP dihole spacetime were reported: there are multiple marginally stable circular orbits of massive particles [41] and the stable circular photon orbit appears [42]. Our studies [43,44] have been strongly inspired by [41]. The authors of [41] investigated circular orbits around the axis of symmetry of the MP dihole spacetime in the equal mass and the different mass cases. They classified a parameter range of the MP dihole spacetime focusing on the circular orbits' appearance when varying the mass of two black holes. However, their analysis had been incomplete, and they missed some distinctive appearances of circular orbits. In contrast, we study circular orbits in the MP dihole spacetime with equal mass and different mass cases and completely classify the parameter ranges of the separation and the mass ratio according to the appearance of the circular orbits. For the equal mass case where the MP dihole spacetime is characterized only by the separation parameter, we find the parameter range of the separation is divided into five parts by four critical values. Since two of these critical values were already reported in [41], we discover two new critical values. At each critical value, the behavior of stable circular orbits drastically changes. We also show the positions of marginally stable circular orbits, ISCOs, and the stable/unstable circular photon orbit for the whole range of the separation parameter. We also investigate the different mass MP dihole spacetime. In this case, the MP dihole spacetime is characterized by not only the separation parameter but also the mass ratio parameter. As the result of our analysis, we divide the mass ratio parameter range into four parts and obtain three critical values as the boundaries. Furthermore, we find some specific behaviors of the circular orbits that do not appear in a single black hole case.

In last year, a very impressive observational result was announced. It is the first image of the black hole shadow of M87* obtained by the Event Horizon Telescope (EHT) Collaboration [7–12]. The EHT results of the shadow distinguish between conflicting mass measurements, favoring that estimated from stellar dynamics [45] rather than that estimated from gas dynamics [46] and suggest that a supermassive black hole may exist at the center of the galaxy. However, the possibility that the central dark object is a horizonless compact object has not yet been ruled out [11,47,48]. In order to distinguish M87* is a black hole or a black hole mimicker, it is necessary to observe the vicinity of the event horizon precisely. Naively, it

seems difficult to observe the near-horizon area of a black hole because in the near-horizon area, the gravity is extremely strong and nothing can escape from the event horizon.

However, according to recent theoretical research progress, in principle, it is possible to overcome this difficulty if a black hole is rapidly rotating. Since the observations of the black hole jet generally expect that M87* has relatively high spin [49] or might be a rapidly rotating black hole [50,51], it is meaningful to pursue phenomena near the horizon of a near-extremal Kerr black hole. It has been shown that some observable features such as bright border of the shadow edge appear in a near-extremal Kerr black hole [52, 53]. More recently, it was explicitly shown that in the extremal Kerr spacetime, for a light source at rest with respect to the locally nonrotating observer, the escape probability of a photon becomes a nonzero value in the limit as the source position approaches the horizon [54, 55].[1] Furthermore, the probability becomes zero in the same limit in the subextremal case, but in the near-extremal case, nonzero value is still achieved just before the horizon. These results indicate that the vicinity of a rapidly rotating black hole is more visible than that of a slowly rotating one.

In general, a light source near a black hole is expected to move relative to the horizon. The second aim of this thesis is to clarify the escape probability of a photon from a light source circularly orbiting near a rapidly rotating black hole. The motion of a light source affects the photon escape probability and the initial energy injection to a photon. In particular, sources moving on stable circular orbits often exist in nature and further provide natural initial conditions for optically observable phenomena [57, 58]. For instance, the apparent shape of the innermost edge of a standard accretion disk surrounding a black hole appears as a closed curve [59–64]. Furthermore, the ISCO radius coincides with the horizon radius in the extremal Kerr spacetime [65, 66], so that the study of revealing the photon emitted from the ISCO can reach infinity in the (near-)extremal Kerr black hole has the insights for the observability of the near-horizon region. One of the additional features of a source on the ISCO in the extremal Kerr spacetime is that the relative velocity to the extremal horizon can get arbitrarily close to half of the speed of light [65]. Emission from this light source yields the boost of each photon and photon concentration in the forward direction of the source by the relativistic

[1] Ratio of photons trapped by a black hole was also discussed in Ref. [56].

beaming. Therefore, it can be expected that the escape probability of a photon emitted from the ISCO of a rapidly rotating black hole becomes relatively large owing to the boost effect. In fact, we show that in the extremal Kerr black hole, the escape probability of a photon for the light source orbiting on the ISCO is 54.6%. This value is greater than 29.1% that is the escape probability for the light source at rest with respect to a locally nonrotating observer obtained in [55]. This amplification of the escape probability comes from the boost effect due to the light source's circular motion. We also show that the photons emitted forwardly get blueshifted for a distant observer.

This thesis is based on our works [43, 44, 67] during doctoral course. The contents of this thesis are as follows:

Chapter 2

We briefly review circular orbits of test particles in the Schwarzschild spacetime and the Kerr spacetime. We introduce an effective potential for a test particle and see that the positions of the circular orbits correspond to the local extrema of an effective potential. In the Kerr spacetime, we also see the position of the circular orbit depends on the Kerr parameter, and the radii of the circular photon orbit and the ISCO coincide with the horizon radius in the extremal black hole limit.

Chapter 3

We study the effect of a second compact object on the circular orbits using the Majumdar–Papapetrou dihole spacetime, which consists of two extremal Reissner–Nordström black holes. We show that the sequence of the stable circular orbit depends on the separation and the mass ratio. We also show that some properties that do not appear in a single black hole arise in the Majumdar–Papapetrou dihole spacetime. This chapter is based on K. Nakashi and T. Igata, "Innermost stable circular orbits in the Majumdar-Papapetrou dihole spacetime," Phys. Rev. D **99**, no.12, 124033 (2019) [43] and K. Nakashi and T. Igata, "Effect of a second compact object on stable circular orbits," Phys. Rev. D **100**, no.10, 104006 (2019) [44].

Chapter 4

We estimate the escape probability of a photon from the vicinity of the event

horizon of the (near-)extremal Kerr black hole. We consider an isotropically emitting particle on the circular orbit as a light source. In the extremal black hole, even if the orbital radius of the light source is arbitrarily close to the ISCO radius, which coincides with the horizon radius, the escape probability approaches nonzero value. We also show that such photons that have escaped from the vicinity of the horizon reach infinity with sufficient energy to be potentially observed. This chapter is based on T. Igata, K. Nakashi and K. Ogasawara, "Observability of the innermost stable circular orbit in a near-extremal Kerr black hole," Phys. Rev. D **101**, no.4, 044044 (2020) [67].

Chapter 5

We summarize the conclusions and the discussions.

In this thesis, we use the following conventions: the metric signature $(-,+,+,+)$; the units in which $G = 1$ and $c = 1$.

Chapter 2

Geodesics and Circular orbits in black hole spacetimes

In this chapter, we briefly review circular orbits of particles around two famous black hole spacetimes, i.e, the Schwarzschild spacetime and the Kerr spacetime.

2.1 Schwarzschild spacetime

2.1.1 Nature of the Schwarzschild spacetime

The metric of the Schwarzschild spacetime is given by

$$\mathrm{d}s^2 = -f(r)\mathrm{d}t^2 + f(r)^{-1}\mathrm{d}r^2 + r^2\left(\mathrm{d}\theta^2 + \sin^2\theta\mathrm{d}\phi^2\right), \tag{2.1}$$

$$f(r) = 1 - \frac{2M}{r} \tag{2.2}$$

where M is the mass of the black hole. We set $M = 1$ in what follows. Due to the static and spherical symmetries of the Schwarzschild spacetime, there are two Killing vectors $\xi^\mu = (\partial_t)^\mu$ and $\psi^\mu = (\partial_\phi)^\mu$. The Schwarzschild metric is singular at $r = 2$ and $r = 0$. At $r = 0$, the spacetime geometry is singular. Indeed, the Kretschmann invariant $R_{\mu\nu\rho\lambda}R^{\mu\nu\rho\lambda}$ diverges at $r = 0$.

We show that the singularity of the Schwarzschild metric at $r = 2$ is just coordinate singularity by investigating the causal structure of the spacetime. Because of the spherical symmetry, the two-dimensional (t, r) part is important for analyzing the causal structure.

First, we introduce the *Eddington–Finkelstein coordinates* u and v as

$$u = t - r_*, \quad (-\infty < u < \infty) \tag{2.3}$$

$$v = t + r_*, \quad (-\infty < v < \infty) \tag{2.4}$$

where r_* is the *tortoise coordinate* expressed as

$$r_* = \int \frac{\mathrm{d}r}{f(r)} = r + 2\log\left|\frac{r}{2} - 1\right|, \tag{2.5}$$

where we set an integration constant so that $r_* = 0$ at $r = 0$. The singularity at $r = 2$ corresponds to $r_* = -\infty$. The ingoing radial null particles move along $v =$ const. line, while the outgoing radial null particles move along $u =$ const. line. In the Eddington–Finkelstein coordinates, the metric (2.2) becomes

$$\mathrm{d}s^2 = -\frac{2e^{-r/2}}{r} e^{(v-u)/4} \mathrm{d}u\mathrm{d}v. \tag{2.6}$$

Since the tortoise coordinate can be expressed in terms of the Eddington–Finkelstein coordinate as $r_* = (v - u)/2$, the singularity at $r = 2$ is still singularity.

Next, we introduce the new coordinates for $r > 2$ so-called the *Kruskal coordinates* U and V as

$$U = -e^{-u/4}, \quad V = e^{v/4}. \tag{2.7}$$

In terms of these coordinates, the metric becomes

$$\mathrm{d}s^2 = -\frac{32}{r} e^{-r/2} \mathrm{d}U\mathrm{d}V. \tag{2.8}$$

This metric is regular at $r = 2$. This means that the singularity at $r = 2M$ in Eq. (2.2) is just a coordinate singularity. Initially the metric is defined for $U < 0$ and $V > 0$, but it can be extended for $U > 0$ and $V < 0$. The relation between (U, V) and r is given by

$$UV = -\left(\frac{r}{2} - 1\right) e^{r/2}. \tag{2.9}$$

In the Kruskal coordinates, $r =$ const. curves appear as $UV =$ const. curves. For example, $r = 2$ becomes $UV = 0$ and $r = 0$ becomes $UV = 1$. Figure 2.1 shows the Kruskal diagram. In Fig. 2.1, the region I corresponds to the original exterior

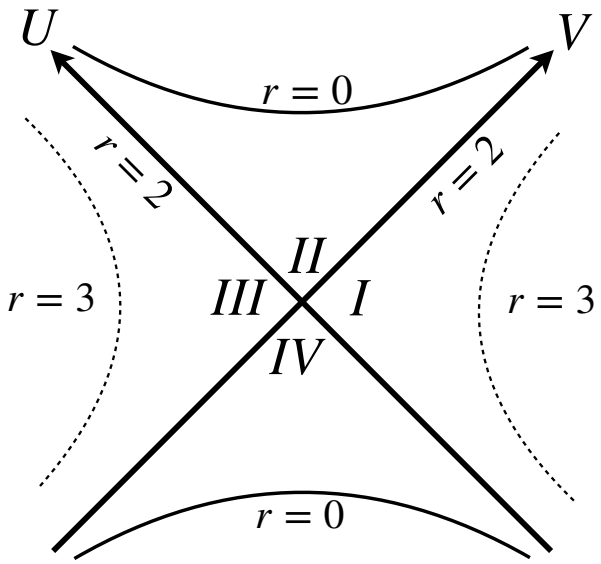

Figure 2.1: Kruskal diagram

region $r > 2$. A radially infalling observer in region I can enter the region II. Once the observer enters the region II, the observer cannot escape from this region. In this sense, we can interpret that the radius $r = 2$ is a horizon. In the Schwarzschild spacetime, the radius $r = 2$ is the event horizon and the Killing horizon. In fact, it is known that the Killing vector ξ^μ is null on the $r = 2$ surface and tangent to the horizon generator.

2.1.2 Geodesics in the Schwarzschild spacetime

The Lagrangian of a freely falling particle is given by

$$\mathcal{L} = \frac{1}{2} g_{\mu\nu} \dot{x}^\mu \dot{x}^\nu = \frac{1}{2} \left[-f(r)\dot{t}^2 + \frac{\dot{r}^2}{f(r)} + r^2 \dot{\theta}^2 + r^2 \sin^2\theta \dot{\phi}^2 \right], \tag{2.10}$$

where the dot denotes the derivative with respect to an affine parameter. The θ-component of the Euler–Lagrange equation becomes

$$\ddot{\theta} = \dot{\phi} \sin\theta \cos\theta - \frac{2\dot{r}\dot{\theta}}{r}. \tag{2.11}$$

This equation means that the orbits that travel on the equatorial plane $\theta = \pi/2$ at the initial moment t_i remain to be restricted to the equatorial plane because

$\ddot{\theta}(t_i) = 0$ for such orbits. For this reason, we focus on the orbits moving on the equatorial plane without loss of generality.

Since the spacetime is static and spherical symmetry, the Lagrangian is independent of the coordinates t and ϕ. Thus, there are two conserved quantities as follows

$$E = f(r)\dot{t}, \quad L = r^2\dot{\phi}. \tag{2.12}$$

These quantities are the particle's energy and the particle's angular momentum, respectively. We assume that the worldline is parametrized so that $g_{\mu\nu}\dot{x}^\mu\dot{x}^\nu = -\kappa$, where $\kappa = 1$ for a timelike particle and $\kappa = 0$ for a massless particle. From this normalization and Eqs. (2.12), we introduce the effective potential $V(r)$ as

$$\dot{r}^2 + V(r) = E^2, \tag{2.13}$$

$$V(r) = f(r)\left(\kappa + \frac{L^2}{r^2}\right). \tag{2.14}$$

We consider a circular orbit with constant r. A particle in a circular orbit must satisfy the following conditions: (a) $\dot{r} = 0$ and (b) $\ddot{r} = 0$. The condition (a) together with Eq. (2.13) leads to

$$V(r) = E^2. \tag{2.15}$$

Conditions (a),(b), and Eq. (2.15), together with the equation of motion for radial direction imply

$$V_r = 0, \tag{2.16}$$

where $V_r = \mathrm{d}V(r)/\mathrm{d}r$. The location of a circular orbit corresponds to that of a stationary point of the effective potential at which the values of the effective potential are positive.

For massless particles ($\kappa = 0$), the condition (2.16) has only one root

$$r_{\mathrm{pc}} = 3. \tag{2.17}$$

This is the radius of the circular photon orbit. The stability of the circular photon orbit is unstable because $V_{rr}(r_{\mathrm{pc}}) < 0$. For timelike particles ($\kappa = 1$), the effective potential becomes

$$V(r) = 1 - \frac{2}{r} + \frac{L^2}{r^2} - \frac{2L^2}{r^3}. \tag{2.18}$$

Note that $2/r$ and L^2/r^2 terms are the Newtonian effect and the centrifugal force effect, respectively, while $2L^2/r^3$ term can be interpreted as the general relativity effect. Because of this general relativity effect, the effective potential has a local maximum, which corresponds to an unstable circular orbit. It is said that the unstable circular orbit around the Schwarzschild black hole reflect the nonlinear effect of the gravity because the unstable circular orbit does not appear in Newtonian gravity. The inner boundary of the existence range of unstable circular orbits is the circular photon orbit: $r = 3$. The condition (2.16) has the roots

$$r_{\mathrm{tc}\pm} = \frac{L^2 \pm \sqrt{L^2(L^2-12)}}{2}. \tag{2.19}$$

We note that the larger root $r_{\mathrm{tc}+}$ is a local minimum of the effective potential, while the smaller root $r_{\mathrm{tc}-}$ is a local maximum. The radius of the circular orbit for a timelike particle depends on the angular momentum. In the case of $L^2 = 12$, the radii of the stable and the unstable circular orbits coincide with each other, and then the radius is given by

$$r_{\mathrm{I}} = 6. \tag{2.20}$$

This radius is the minimum radius of a stable circular orbit. There is no stable circular orbits inside it, and it is called the innermost stable circular orbit (ISCO). The ISCO often plays key roles for some astrophysical phenomena. For example, it is expected to be the inner edge of an accretion disk [17], and also an inspiralling compact binary transits into the merging phase there [18, 19].

2.2 Kerr spacetime

2.2.1 Nature the Kerr spacetime

The metric of the Kerr spacetime in the Boyer–Lindquist coordinate $\{t, r, \theta, \phi\}$ is given by

$$\mathrm{d}s^2 = -\frac{\Sigma\Delta}{A}\mathrm{d}t^2 + \frac{\Sigma}{\Delta}\mathrm{d}r^2 + \Sigma\mathrm{d}\theta^2 + \frac{A}{\Sigma}\sin^2\theta\left[\mathrm{d}\varphi - \frac{a(r^2+a^2-\Delta)}{A}\mathrm{d}t\right]^2, \tag{2.21}$$

$$\Sigma = r^2 + a^2\cos^2\theta, \quad \Delta = r^2 + a^2 - 2Mr, \quad A = (r^2+a^2)^2 - \Delta a^2\sin^2\theta, \tag{2.22}$$

where M is the mass of the black hole and a is the Kerr parameter defined as the magnitude of the angular momentum of the black hole divided by the mass. As in the case of the Schwarzschild spacetime, we set $M = 1$ in what follows. Because of the stationary and axisymmetry of the Kerr spacetime, there are two Killing vectors $\xi^\mu = (\partial_t)^\mu$ and $\psi^\mu = (\partial_\phi)^\mu$. The metric (2.21) has two singularities such that $\Delta = 0$ and $\Sigma = 0$. The former singularity is just coordinate singularity and the roots of $\Delta = 0$ correspond to the outer/inner horizon:

$$r_\pm = 1 \pm \sqrt{1 - a^2}. \tag{2.23}$$

From this expression, we can read that there exist the horizons for $a^2 \leq 1$. We assume $0 \leq a \leq 1$ throughout this thesis. Since the later singularity corresponds to the curvature singularity, the Kerr spacetime is truly singular at $\Sigma = 0$.

To discuss the nature of the Kerr spacetime in more detail, we consider two specific observers: a static observer and a stationary observer. The four-velocity u^μ of a static observer is proportional to the Killing vector ξ^μ:

$$u^\mu = \frac{\xi^\mu}{\sqrt{-g_{\mu\nu}\xi^\mu\xi^\nu}}. \tag{2.24}$$

Note that orbits of the static observers are not geodesics. At spatial infinity, the four-velocity of a static observer is timelike. However, in the Kerr spacetime, there is a surface on which the four-velocity of a static observer becomes null. This surface is called the ergosurface. Static observers cannot exist inside the ergosurface because the four-velocity (2.24) is spacelike. The position of the ergosurface is obtained from $g_{\mu\nu}\xi^\mu\xi^\nu = g_{tt} = 0$ as

$$r_{\rm E}(\theta) = 1 + \sqrt{1 - a^2\cos^2\theta}. \tag{2.25}$$

Next, we consider a stationary observer whose four-velocity is given by

$$u^\mu = \frac{\xi^\mu + \Omega\,\psi^\mu}{\sqrt{-g_{\phi\phi}(\Omega^2 - 2\omega\Omega + g_{tt}/g_{\phi\phi})}}, \tag{2.26}$$

where $\Omega = {\rm d}\phi/{\rm d}t$ and $\omega = -g_{t\phi}/g_{\phi\phi}$, respectively. The condition for the presence of the timelike stationary observer restricts the range of the angular momentum of the observer. The allowed range is given by

$$\Omega_- < \Omega < \Omega_+, \tag{2.27}$$

where

$$\Omega_{\pm} = \omega \pm \sqrt{\omega^2 - \frac{g_{tt}}{g_{\phi\phi}}}. \tag{2.28}$$

The boundary values $\Omega_{\pm}$ are coincide with each other when $\Delta = 0$. As we mentioned above, the roots of $\Delta = 0$ are outer/inner horizon of the Kerr spacetime. Thus, the vector $\xi^\mu + \Omega\psi^\mu$ becomes null at these horizons and the stationary observer cannot exist between these horizons. We find that the vector

$$\chi^\mu = \xi^\mu + \Omega_{\rm H}\psi^\mu, \tag{2.29}$$

is null on the outer horizon, where

$$\Omega_{\rm H} = \left.\frac{{\rm d}\phi}{{\rm d}t}\right|_{r=r_+} = \frac{a}{r_+^2 + a^2}, \tag{2.30}$$

is the angular velocity of the black hole horizon. Because the vector χ^μ is a linear combination of two Killing vectors, it is also a Killing vector. In addition, the vector χ^μ is the horizon generator. The remarkable difference between static and stationary black holes is that for static black holes, ξ^μ becomes null on the event horizon, while for stationary black holes, ξ^μ is null on the ergosurface and χ^μ becomes null on the event horizon.

It is worth to mention the circularity of the Kerr spacetime. A stationary and axisymmetric spacetime is said to be *circular* if the two-dimensional planes orthogonal to two commuting Killing vector fields associated with the stationarity and axisymmetry are integrable. An asymptotically flat, stationary, and axisymmetric spacetime is circular if and only if the following circularity conditions are satisfied

$$\psi^\mu R_{\mu[\nu}\,\psi_\rho\,\xi_{\lambda]} = 0, \quad \xi^\mu R_{\mu[\nu}\,\xi_\rho\,\psi_{\lambda]} = 0, \tag{2.31}$$

where ψ^μ and ξ^μ are a spacelike Killing vector whose orbits are closed and an asymptotically timelike Killing vector, respectively. Because the Kerr spacetime is a Ricci flat, the circularity conditions are automatically satisfied: the Kerr spacetime is circular. In general relativity, it is shown that the circularity condition holds for the asymptotically flat spacetimes in vacuum system (see, e.g., [68, 69]), the Einstein real scalar system [70], and Einstein–Maxwell system [71]. Yet, in modified gravity theories, it is not obvious whether spacetimes satisfy the circularity condition or not. If we can observe the effect of non-circularity, it suggests the

violation of general relativity because the circularity condition should hold for general relativity. We have discussed the possibility of the violation of the spacetime circularity in two string-inspired gravity theories [72]. We have shown that in both gravity theories, up to linear order in the coupling constant and quadratic order in the spin, regular non-circular black hole solutions do not exist at least around the Schwarzschild spacetime. Our results suggest the non-existence of rotating non-circular black holes in these gravity theories.

2.2.2 Equatorial geodesics

To see behaviors of circular orbits of test particles, we focus on the orbits in the equatorial plane: $\theta = \pi/2$. Then, the Lagrangian for a test particle becomes

$$2\mathcal{L} = -\left(1 - \frac{2}{r}\right)\dot{t}^2 + \frac{r^2}{\Delta}\dot{r}^2 - \frac{4a}{r}\dot{t}\dot{\phi} + \left[r^2 + a^2 + \frac{2a^2}{r}\right]\dot{\phi}^2, \tag{2.32}$$

where dot denotes the derivative with respect to an affine parameter. Due to the stationarity and the axisymmetry of the Kerr spacetime, there are two constants of motion as follows

$$E = -k_t = \left(1 - \frac{2}{r}\right)\dot{t} + \frac{2a}{r}\dot{\phi}, \tag{2.33}$$

$$L = k_\phi = -\frac{2a}{r}\dot{t} + \left(r^2 + a^2 + \frac{2a^2}{r}\right)\dot{\phi}. \tag{2.34}$$

These constants of motion E and L are the energy of a test particle and the angular momentum of a test particle, respectively. By using these constants of motion, the Hamiltonian is given by

$$2\mathcal{H} = -E\,\dot{t} + L\,\dot{\phi} + \frac{r^2}{\Delta}\dot{r}^2 = -\kappa, \tag{2.35}$$

where $\kappa = 1$ for a timelike particle and $\kappa = 0$ for a massless particle. Solving Eqs. (2.33) and (2.34) for $\dot{t}$ and $\dot{\phi}$, we obtain

$$\dot{t} = \frac{1}{\Delta}\left[\left(r^2 + a^2 + \frac{2a^2}{r}\right)E - \frac{2a}{r}L\right], \tag{2.36}$$

$$\dot{\phi} = \frac{1}{\Delta}\left[\frac{2a}{r}E + \left(1 - \frac{2}{r}\right)L\right]. \tag{2.37}$$

Substituting these expressions into Eq. (2.35), we obtain the equation of motion in the radial direction as

$$\dot{r}^2 = E^2 + \frac{2}{r^3}(aE - L)^2 + \frac{1}{r^2}(a^2E^2 - L^2) - \frac{\kappa\Delta}{r^2}. \tag{2.38}$$

For null geodesics, $\kappa = 0$ and Eq. (2.38) becomes

$$\dot{r}^2 = E^2 + \frac{2}{r^3}(aE - L)^2 + \frac{1}{r^2}(a^2E^2 - L^2). \tag{2.39}$$

For convenience in the below discussion, we calculate $\ddot{r}$

$$\ddot{r} = -\frac{3}{r^4}(aE - L)^2 - \frac{1}{r^3}(a^2E^2 - L^2). \tag{2.40}$$

The conditions determining the radius of the circular photon orbit $r_{\rm pc}$ are $\dot{r} = 0$ and $\ddot{r} = 0$. The radii of circular photon orbits are given by

$$r_{\rm pc}^{\mp} = 2\left[1 + \cos\left(\frac{2}{3}\cos^{-1}(\mp a)\right)\right], \tag{2.41}$$

where the upper sign and lower sign correspond to the direct orbits and the retrograde orbits, respectively. For $a = 0$, $r_{\rm pc}^{+} = r_{\rm pc}^{-} = 3$, which corresponds to the circular photon orbit in the Schwarzschild spacetime, while for $a = 1$, $r_{\rm pc}^{+} = 4$ (retrograde orbit) or $r_{\rm pc}^{-} = 1$ (direct orbit). The all circular photon orbits in the Kerr spacetime are unstable. We note that the coordinate value of $r_{\rm pc}$ for the extremal black hole coincides with the horizon radius.

For timelike geodesics, $\kappa = 1$ and Eq. (2.38) can be written as

$$\dot{r}^2 + V_{\rm eff}(r) = E^2, \tag{2.42}$$

where

$$V_{\rm eff}(r) = -\frac{2}{r^3}(aE - L)^2 - \frac{1}{r^2}(a^2E^2 - L^2) + \frac{\Delta}{r^2}. \tag{2.43}$$

is the effective potential. The conditions determining the radius of a circular orbit $r_{\rm tc}$ are $\dot{r} = 0$ and $\ddot{r} = 0$. These conditions imply that for a circular orbit

$$V_{\rm eff}(r_{\rm tc}) = E^2 \geq 0, \quad \frac{{\rm d}V_{\rm eff}}{{\rm d}r}(r_{\rm tc}) = 0, \tag{2.44}$$

respectively. By solving these equations for E and L, we find

$$E_{\rm tc} = \frac{r_{\rm tc}^{3/2} - 2r_{\rm tc}^{1/2} \pm a}{r_{\rm tc}^{3/4}(r_{\rm tc}^{3/2} - 3r_{\rm tc}^{1/2} \pm 2a)^{1/2}}, \tag{2.45}$$

$$L_{\rm tc} = \frac{\pm(r_{\rm tc}^{2} \mp 2ar_{\rm tc}^{1/2} + a^2)}{r_{\rm tc}^{3/4}(r_{\rm tc}^{3/2} - 3r_{\rm tc}^{1/2} \pm 2a)^{1/2}}, \tag{2.46}$$

where the upper sign and the lower sign correspond to the direct orbit and the retrograde orbit, respectively. The circular orbits cannot exist for all values of r because of the strong gravity effect. The existence range of the circular orbits are determined by the following condition

$$r_{\rm tc}^{3/2} - 3r_{\rm tc}^{1/2} \pm 2a \geq 0. \tag{2.47}$$

If this condition is satisfied, $E_{\rm tc}$ and $L_{\rm tc}$ are real. The inner boundary of the existence range of the circular orbits is the circular photon orbit $r_{\rm pc}$. Unlike the circular photon orbits, the circular orbits of timelike particles exist not only unstable ones but also stable ones. The stable circular orbits satisfy $\mathrm{d}^2V_{\rm eff}(r_{\rm tc})/\mathrm{d}r^2 \geq 0$. This condition can be written as

$$r_{\rm tc}^{2} - 3a^2 - 6r_{\rm tc} \pm 8ar_{\rm tc}^{1/2} \geq 0. \tag{2.48}$$

When the equal sign holds, the root of the equation is the radius of the ISCO because the position of the ISCO corresponds to the inflection point of $V_{\rm eff}$. The ISCO radius in the Kerr spacetime is given by

$$r_{\rm I} = M\{3 + Z_2 \mp \sqrt{(3 - Z_1)(3 + Z_1 + 2Z_2)}\}, \tag{2.49}$$

where

$$Z_1 = 1 + \left(1 - a^2\right)^{1/3}\left[(1 + a)^{1/3} + (1 - a)^{1/3}\right], \tag{2.50}$$

$$Z_2 = \sqrt{3a^2 + Z_1^2}. \tag{2.51}$$

The stable circular orbits exist in the range $r \geq r_{\rm I}$. For $a = 0$, $r_{\rm I} = 6$, while for $a = 1$, $r_{\rm I} = 9$ (retrograde orbits) or $r_{\rm I} = 1$ (direct orbits). Note that similar to the circular photon orbit, the coordinate value of $r_{\rm I}$ coincides with the horizon radius in the extremal black hole case. Figure 2.2 shows the radii of $r_{\rm pc}^{\pm}$ and $r_{\rm I}$ as functions of the Kerr parameter.

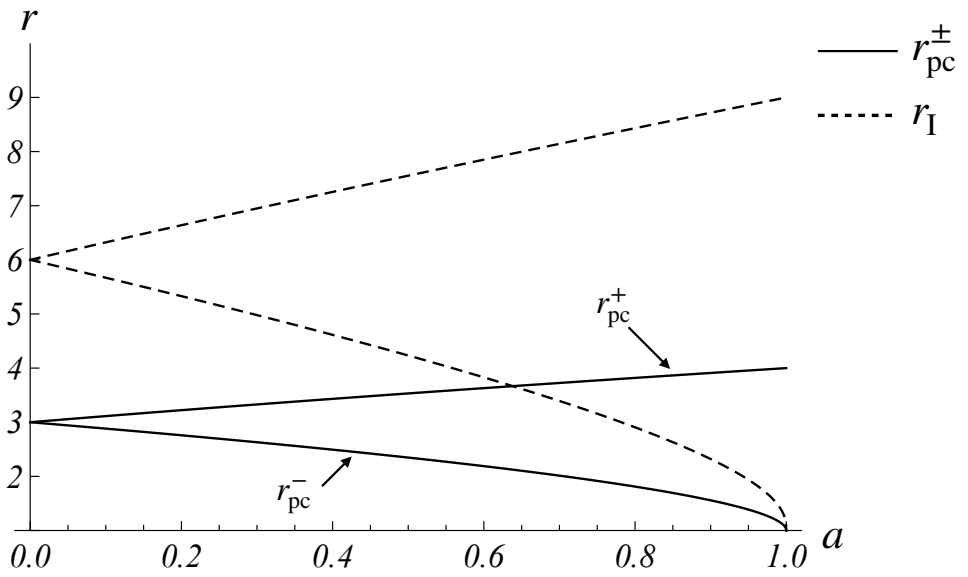

Figure 2.2: Dependence of the radii of the circular photon orbit (solid line) and the ISCO (dashed line) on the Kerr parameter. In the extremal black hole case ($a = 1$), the coordinate values of these coincide with the horizon radius.

2.2.3 General geodesics

We discuss the general geodesic. We show that the separability of the Hamilton–Jacobi equation in the Kerr spacetime. The separability of the Hamilton–Jacobi equation was shown in [73]. The Lagrangian of a test particle is given by

$$2\mathcal{L} = -\left(1 - \frac{2r}{\Sigma}\right)\dot{t}^2 + \frac{\Sigma}{\Delta}\dot{r}^2 + \Sigma\,\dot{\theta}^2 - \frac{4ar\sin^2\theta}{\Sigma}\dot{t}\dot{\phi} + \frac{A\sin^2\theta}{\Sigma}\dot{\phi}^2. \tag{2.52}$$

From this Lagrangian, we obtain the generalized momentum k_μ and the Hamiltonian $\mathcal{H}$ as follows

$$-k_t = \left(1 - \frac{2r}{\Sigma}\right)\dot{t} + \frac{2ar\sin^2\theta}{\Sigma}\dot{\phi}, \tag{2.53}$$

$$k_\phi = -\frac{2ar\sin^2\theta}{\Sigma}\dot{t} + \frac{A\sin^2\theta}{\Sigma}\dot{\phi}, \tag{2.54}$$

$$k_r = \frac{\Sigma}{\Delta}\dot{r}, \tag{2.55}$$

$$k_\theta = \Sigma\,\dot{\theta}, \tag{2.56}$$

$$2\mathcal{H} = g^{\mu\nu}k_\mu k_\nu = -\frac{A}{\Sigma\Delta}k_t^2 + \frac{\Delta}{\Sigma}k_r^2 + \frac{1}{\Sigma}k_\theta^2 + \frac{4ar}{\Sigma\Delta}k_t k_\phi + \frac{\Delta - a^2\sin^2\theta}{\Sigma\Delta\sin^2\theta}k_\phi^2. \tag{2.57}$$

The four constants of motion necessary to make the Hamilton–Jacobi equation separable can be derived by the usual method. From the spacetime symmetry, we can obtain the conserved energy E and the conserved angular momentum L as

$$k_t = -E, \quad k_\phi = L. \tag{2.58}$$

Since the Hamiltonian does not depend on an affine parameter λ explicitly, it is constant:

$$\mathcal{H} = -\frac{\kappa}{2}, \tag{2.59}$$

where $\kappa = 0$ for a null geodesic, while $\kappa = 1$ for a timelike geodesic. The Hamilton–Jacobi equation is given by

$$2\frac{\partial S}{\partial\lambda} = g^{\mu\nu}\frac{\partial S}{\partial x^\mu}\frac{\partial S}{\partial x^\nu}, \tag{2.60}$$

where S is the Hamilton's principle function. If there are separable solutions, the Hamilton's principle function can be written in terms of the known three constants as follows

$$S = -\frac{1}{2}\kappa\lambda - Et + L\phi + S_r(r) + S_\theta(\theta). \tag{2.61}$$

Substituting Eq. (2.61) into Eq. (2.60), we obtain

$$\begin{aligned}&\Delta\left(\frac{\mathrm{d}S_r}{\mathrm{d}r}\right)^2 - \frac{1}{\Delta}\left[(r^2+a^2)E - aL\right]^2 + \kappa r^2 \\ &= -\left(\frac{\mathrm{d}S_\theta}{\mathrm{d}\theta}\right)^2 - (aE\sin^2\theta - L^2)^2\csc^2\theta - \kappa a^2\cos^2\theta.\end{aligned} \tag{2.62}$$

Both sides are equal to a same constant because the left hand side is the function of r, while the right hand side is the function of θ. By using the relations $\mathrm{d}S_r/\mathrm{d}r = k_r$ and $\mathrm{d}S_\theta/\mathrm{d}\theta = k_\theta$, we have

$$\Delta\, k_r^2 - \frac{1}{\Delta}\left[(r^2+a^2)E - aL\right]^2 + \kappa r^2 = -K, \tag{2.63}$$

$$k_\theta^2 + (aE\sin^2\theta - L^2)^2\csc^2\theta + \kappa a^2\cos^2\theta = K, \tag{2.64}$$

where K is a separation constant and this constant is the fourth constant. It can be shown that K is constant because the Poisson's bracket with the Hamiltonian vanishes. In addition, the nontrivial constant K relates to the hidden symmetry in the Kerr spacetime [74]. The Kerr spacetime has a conformal Killing tensor that is a rank two symmetric tensor $K_{\mu\nu}$ satisfying

$$\nabla_{(\rho}K_{\mu\nu)} = 0. \tag{2.65}$$

and in the Kerr spacetime, it is expressed as

$$\begin{aligned} K_{\mu\nu}\mathrm{d}x^\mu\mathrm{d}x^\nu = \Sigma^2\mathrm{d}\theta^2 - a^2\cos^2\theta g_{\mu\nu}\mathrm{d}x^\mu\mathrm{d}x^\nu \\ + \sin^2\theta\left[(r^2+a^2)\mathrm{d}\varphi - a\mathrm{d}t\right]\left[(r^2+a^2)\mathrm{d}\varphi - a\mathrm{d}t\right]. \end{aligned} \tag{2.66}$$

By using the Killing tensor, the nontrivial constant K can be expressed as $K = K_{\mu\nu}\,k^\mu\,k^\nu$.

From the above discussion, the Hamilton's principle function is given by

$$S = -\frac{1}{2}\kappa\lambda - Et + L\phi\int^r\frac{\sqrt{R}}{\Delta}\mathrm{d}r + \int^\theta\sqrt{\Theta}\mathrm{d}\theta, \tag{2.67}$$

where

$$R(r) = \left[(r^2+a^2)E - aL\right]^2 - \Delta\left[\kappa r^2 + Q + (L-aE)^2\right], \tag{2.68}$$

$$\Theta(\theta) = Q - \cos^2\theta\left[a^2(\kappa - E^2) + L^2\csc^2\theta\right], \tag{2.69}$$

$$Q = K - (L-aE)^2. \tag{2.70}$$

Here, we introduce a constant Q, so-called the *Carter constant*. From Eqs. (2.58), (2.63), and (2.64), we obtain the geodesic equations:

$$\Sigma\,\dot{r} = \pm\sqrt{R(r)}, \tag{2.71}$$

$$\Sigma\,\dot{\theta} = \pm\sqrt{\Theta(\theta)}, \tag{2.72}$$

$$\Sigma\,\dot{t} = a(L - aE\sin^2\theta) + \frac{r^2+a^2}{\Delta}[(r^2+a^2)E - aL], \tag{2.73}$$

$$\Sigma\,\dot{\phi} = L\csc^2\theta - aE + \frac{a}{\Delta}[(r^2+a^2)E - aL]. \tag{2.74}$$

• **θ-motion**

We discuss the θ-motion of a geodesic in the Kerr spacetime. Unlike the case of the Schwarzschild spacetime, in the Kerr spacetime, a geodesic can deviate from the equatorial plane. The geodesic motion in θ direction is characterized by the value of the Carter constant Q. According to Eq. (2.72), the geodesic equation in θ direction has real solutions only for $\Theta = Q - \cos^2\theta\left[a^2(\kappa - E^2) + L^2\csc^2\theta\right] \geq 0$. When $Q > 0$, the function has a zero point at the points θ_0 and $\pi - \theta_0$, and it is positive in this interval containing the equatorial plane. This means the geodesics can across the equatorial plane and they oscillate symmetrically. When $Q < 0$, the a geodesic confined to a cone and cannot intersect the equatorial plane. When $Q = 0$, real roots always exist for $\theta = \pi/2$: this case corresponds to the equatorial geodesics.

• **r-motion (null geodesics)**

Here, we discuss null geodesics because in Chapter 4, we use only null geodesics for the analysis. We introduce two impact parameters as

$$b = \frac{L}{E}, \quad q = \frac{Q}{E^2}, \tag{2.75}$$

Then the geodesic equations are written in terms b and q as follows

$$k^t\dot{t} = \frac{1}{\Sigma}\left[a\left(b - a\sin^2\theta\right) + \frac{r^2+a^2}{\Delta}\left(r^2 + a^2 - ab\right)\right], \tag{2.76}$$

$$k^r = \dot{r} = \frac{\sigma_r}{\Sigma}\sqrt{R}, \tag{2.77}$$

$$k^\theta = \dot{\theta} = \frac{\sigma_\theta}{\Sigma}\sqrt{\Theta}, \tag{2.78}$$

$$k^\varphi = \dot{\varphi} = \frac{1}{\Sigma}\left[\frac{b}{\sin^2\theta} - a + \frac{a}{\Delta}\left(r^2 + a^2 - ab\right)\right], \tag{2.79}$$

where σ_r, $\sigma_\theta = \pm$, the dot denotes the derivative with respect to an affine parameter, and

$$R = \left(r^2 + a^2 - ab\right)^2 - \Delta\left[q + (b-a)^2\right], \tag{2.80}$$

$$\Theta = q - b^2\cot^2\theta + a^2\cos^2\theta. \tag{2.81}$$

According to these geodesic equations, we can find that the null geodesics in the Kerr spacetime are completely characterized by b and q.

We focus on the spherical photon orbit [75]. The spherical photon orbit is a characteristic orbit in the Kerr spacetime and relates various phenomena and observations such as the black hole shadow. The locations of the spherical photon orbits are determined by following two equations

$$R = 0, \quad \frac{\mathrm{d}R}{\mathrm{d}r} = 0. \tag{2.82}$$

Solving these equations for b and q, we obtain

$$b_{\rm sp} = \frac{(r_{\rm sp}-3)r_{\rm sp}^2 + a^2(r_{\rm sp}+1)}{a(1-r_{\rm sp})}, \tag{2.83}$$

$$q_{\rm sp} = -\frac{r_{\rm sp}^3(r_{\rm sp}(r_{\rm sp}-3)^2 - 4a^2)}{a^2(r_{\rm sp}-1)^2}. \tag{2.84}$$

The radius of the spherical photon orbit is determined by these quantities implicitly. For $q_{\rm sp} = 0$, the radii of the spherical photon orbits are the roots of the following equation

$$r^{3/2} - 3r^{1/2} \pm 2a = 0. \tag{2.85}$$

This is the equation giving the radius the circular photon orbit $r_{\rm pc}$. The radius is given by Eq. (2.41). For $q > 0$, the radius of the spherical photon orbit is restricted in the range $r_{\rm pc}^- < r_{\rm sp} < r_{\rm pc}^+$.

Chapter 3

Effect of a second compact object on stable circular orbit

The contents of this chapter is originally published as:

• K. Nakashi and T. Igata, "Innermost stable circular orbits in the Majumdar-Papapetrou dihole spacetime," Phys. Rev. D **99** (2019) no.12, 124033,

• K. Nakashi and T. Igata, "Effect of a second compact object on stable circular orbits," Phys. Rev. D **100** (2019) no.10, 104006.

In this chapter, we study the effect of a second compact object on the stable circular orbits using the Majumdar–Papapetrou (MP) dihole spacetime. We show that in the MP dihole spacetime, the appearances of the circular orbits of test particles are different from those of a single black hole. We classify the parameter range of the separation and the mass ratio according to the qualitative changes of the stable circular orbits in the MP dihole spacetime. We also discuss some properties of the sequence of the stable circular orbits, which do not appear in a single black hole, and the expected phenomena.

3.1 Conditions for stable circular orbits in the Majumdar–Papapetrou dihole spacetime

The metric and the gauge field of the MP dihole spacetime in isotropic coordinates are given by

$$g_{\mu\nu}\mathrm{d}x^\mu \mathrm{d}x^\nu = -\frac{\mathrm{d}t^2}{U^2} + U^2(\mathrm{d}\rho^2 + \rho^2\mathrm{d}\phi^2 + \mathrm{d}z^2), \tag{3.1}$$

$$A_\mu \mathrm{d}x^\mu = U^{-1}\mathrm{d}t, \tag{3.2}$$

$$U(\rho, z) = 1 + \frac{M_+}{\sqrt{\rho^2 + (z-d)^2}} + \frac{M_-}{\sqrt{\rho^2 + (z+d)^2}}, \tag{3.3}$$

where $M_\pm$ are each black hole mass located at $z = \pm d$ ($d \geq 0$). Note that we choose cylindrical coordinates on the spatial geometry, $x = \rho\cos\phi$ and $y = \rho\sin\phi$, where x, y are the Cartesian coordinates. We introduce a mass ratio parameter

$$\nu := \frac{M_-}{M_+}. \tag{3.4}$$

We assume that the black hole mass M_+ is equal or larger than another black hole mass M_-, i.e.,

$$0 \leq \nu \leq 1. \tag{3.5}$$

We use units in which $M_+ = 1$ in what follows.

The Lagrangian of a particle freely falling in the MP dihole spacetime is given by

$$\mathcal{L} = \frac{1}{2}\left[-\frac{\dot{t}^2}{U^2} + U^2(\dot{\rho}^2 + \rho^2\dot{\phi}^2 + \dot{z}^2)\right], \tag{3.6}$$

where the dot denotes derivative with respect to an affine parameter. Since the coordinates t and ϕ are cyclic, the canonical momenta conjugate to them are constants of motion:

$$E = \frac{\dot{t}}{U^2}, \quad L = \rho^2 U^2 \dot{\phi}, \tag{3.7}$$

which are energy and angular momentum, respectively. We normalize the four-velocity $\dot{x}^\mu$ so that $g_{\mu\nu}\dot{x}^\mu\dot{x}^\nu = -\kappa$, where $\kappa = 1$ for a timelike particle and $\kappa = 0$

for a massless particle. Rewriting the normalization condition in terms of E and L, we have

$$\dot{\rho}^2 + \dot{z}^2 + V = E^2, \tag{3.8}$$

$$V(\rho, z) = \frac{L^2}{\rho^2 U^4} + \frac{\kappa}{U^2}. \tag{3.9}$$

We can view Eq. (3.8) as an energy equation and V as a 2D effective potential of particle motion in the ρ-z plane. In terms of V, the equations of motion are written as

$$\ddot{\rho} + \frac{2U_z}{U}\dot{z}\dot{\rho} - \frac{2U_\rho}{U}\dot{z}^2 + \frac{V_\rho}{2} = 0, \tag{3.10}$$

$$\ddot{z} + \frac{2U_\rho}{U}\dot{z}\dot{\rho} - \frac{2U_z}{U}\dot{\rho}^2 + \frac{V_z}{2} = 0, \tag{3.11}$$

where $V_i = \partial_i V$ and $U_i = \partial_i U$ $(i = \rho, z)$.

We focus on circular orbits with constant ρ and z. Then, the energy equation (3.8) immediately reduces to

$$V = E^2. \tag{3.12}$$

Hence, V must be positive for circular orbits. In addition, we find that constant (ρ, z) can be a solution to Eqs. (3.10) and (3.11) when its position corresponds to an extremum of V:

$$V_\rho = 0, \tag{3.13}$$

$$V_z = 0. \tag{3.14}$$

We can rewrite the three conditions (3.12)–(3.14), respectively, as

$$E^2 = E_0^2(\rho, z) := V(\rho, z; L_0^2), \tag{3.15}$$

$$L^2 = L_0^2(\rho, z) := -\frac{\rho^3 U^2 U_\rho}{U + 2\rho U_\rho}, \tag{3.16}$$

$$U_z = \frac{d - z}{[\rho^2 + (z - d)^2]^{3/2}} - \frac{\nu(d + z)}{[\rho^2 + (z + d)^2]^{3/2}} = 0. \tag{3.17}$$

From Eqs. (3.15) and (3.16), both values of E_0^2 and L_0^2 depend on positions of circular orbits and must be positive. The positivity of L^2 leads to that of E^2 as

seen from Eq. (3.9), so that it is sufficient to pay attention only to the positivity of L^2.

Now we solve Eq. (3.17). If $\nu = 0$, then we obtain the solution $z = d$. If $0 < \nu \leq 1$, we find that from Eq. (3.17), the range of z is bounded in $|z| < d$. Solving Eq. (3.17) for ρ^2 in this range, we obtain the root

$$\rho_0^2(z) = \frac{(d-z)^{2/3}(d+z)^2 - \nu^{2/3}(d+z)^{2/3}(d-z)^2}{\nu^{2/3}(d+z)^{2/3} - (d-z)^{2/3}}, \tag{3.18}$$

for $z \neq d(1-\nu)/(1+\nu)$. When $z = d(1-\nu)/(1+\nu)$ holds, then Eq. (3.17) leads to $z = 0$, and hence $\nu = 1$. Note that the root ρ_0 is real and positive in the range

$$-d < z < -\frac{1-\sqrt{\nu}}{1+\sqrt{\nu}}d, \quad \frac{1-\nu}{1+\nu}d < z < d. \tag{3.19}$$

As the radius increases, the curve [1] $\rho = \rho_0$ approaches the line

$$z = \frac{1-\nu}{1+\nu}\, d. \tag{3.20}$$

On the other hand, the curves terminate on $\rho = 0$ at $z = \pm\, d$ (i.e., the horizons) and

$$z = -\frac{1-\sqrt{\nu}}{1+\sqrt{\nu}}d. \tag{3.21}$$

Note that we can find a circular orbit at a point in the ρ-z plane if it is located on the curve $\rho = \rho_0(z)$ and satisfies $E_0^2 \geq 0$ and $L_0^2 \geq 0$.

To determine the stability of a circular orbit, we need further analysis. From the standard linear stability analysis of circular orbits, we find that a circular orbit is stable if and only if the orbit exists at a local minimum point of V. We call such a circular orbit a stable circular orbit. On the other hand, a circular orbit is unstable if and only if the orbit exists at a local maximum point of V or a saddle point of V. We call such a circular orbit an unstable circular orbit. Here, we introduce the Hessian of V and the trace of $V_{ij} = \partial_i \partial_j V$

$$h(\rho, z; L^2) = \det V_{ij}, \tag{3.22}$$

$$k(\rho, z; L^2) = \mathrm{Tr} V_{ij}. \tag{3.23}$$

[1] Equations (3.18) and (3.20) indeed form hypersurfaces in the spacetime, while these form one-dimensional curves in the ρ-z plane. The words "curve" and "line" used in this chapter mean such one-dimensional curves in the ρ-z plane.

In terms of these quantities, we can summarize the stability of circular orbits as follows:

(i) A circular orbit is stable $\Longleftrightarrow$ $h > 0$ and $k > 0$ at a stationary point of V;

(ii) A circular orbit is unstable $\Longleftrightarrow$ ($h > 0$ and $k < 0$) or $h < 0$ at a stationary point of V.

When a sequence of stable circular orbits switches to a sequence of unstable circular orbits at a radius, we call the circular orbit at the radius a marginally stable circular orbit (MSCO), where V has an inflection point (i.e., $h = 0$). In particular, we call the MSCO with the smallest value of the radial coordinate ρ the innermost stable circular orbit (ISCO). To discuss the stability of circular orbits, we introduce the Hessian h and the trace k evaluated at $L^2 = L_0^2$

$$h_0(\rho, z) = h(\rho, z; L_0^2)|_{U_z=0}, \tag{3.24}$$

$$k_0(\rho, z) = k(\rho, z; L_0^2)|_{U_z=0}, \tag{3.25}$$

where the restriction $U_z = 0$ means that the terms directly proportional to U_z have been removed from the right-hand sides. Using h_0 and k_0, we specify the region where the remaining conditions for stable circular orbits hold

$$D = \{(\rho, z) \,|\, h_0 > 0, k_0 > 0, L_0^2 > 0\}. \tag{3.26}$$

We can find stable circular orbits on the curve $\rho = \rho_0(z)$ included in the region D.

3.2 Equal mass case

In this section, we focus on the equal mass MP dihole spacetime: $\nu = 1$. The equal mass MP dihole spacetime depends on only the separation parameter d. In this case, Eq. (3.17) reduces to

$$z\left[\rho^6 - 3\left(d^2 - z^2\right)^2\rho^2 - 2\left(d^2 + z^2\right)\left(d^2 - z^2\right)^2\right] = 0. \tag{3.27}$$

This equation means that U_z always vanishes on the symmetric plane $z = 0$. Focusing on the case where the inside of the square bracket vanishes, we find another real root of Eq. (3.17)

$$\rho_0^2 = 2(d^2 - z^2)\cos\left[\frac{1}{3}\arccos\frac{d^2 + z^2}{d^2 - z^2}\right]. \tag{3.28}$$

Hence, we obtain two curves $z = 0$ and $\rho = \rho_0(z)$ in ρ-z plane, where U_z vanishes. Note that these curves intersect each other at $(\rho, z) = (\sqrt{2}d, 0)$.

It is convenient to obtain the expressions L_0, E_0, and h_0 evaluated at the symmetric plane $z = 0$. To derive them in simpler forms, we use a new coordinate R defined by

$$R(\rho) = \sqrt{\rho^2 + d^2}, \tag{3.29}$$

where $R \geq d$, which follows from $\rho \geq 0$. In terms of R, we derive angular momentum and energy for a circular orbit on $z = 0$, respectively,

$$L_0(\rho, 0) = \frac{\sqrt{2}(R+2)(R^2 - d^2)}{R\sqrt{F}}, \tag{3.30}$$

$$E_0(\rho, 0) = \frac{R\sqrt{R^3 + 2d^2}}{(R+2)\sqrt{F}}, \tag{3.31}$$

where, without loss of generality, we have chosen the branch $L_0 \geq 0$, and

$$F(R) = R^3 - 2R^2 + 4d^2. \tag{3.32}$$

Note that these quantities diverge if F vanishes. Furthermore, in the range $F < 0$, there is no circular orbit. In addition, the derivatives of $L_0(\rho, 0)$ and $E_0(\rho, 0)$ with respect to R are given by, respectively,

$$\frac{\mathrm{d}L_0(\rho, 0)}{\mathrm{d}R} = \frac{G}{\sqrt{2}R^2F^{3/2}}, \tag{3.33}$$

$$\frac{\mathrm{d}E_0(\rho, 0)}{\mathrm{d}R} = \frac{G}{(R+2)^2\sqrt{R^3 + 2d^2}F^{3/2}}, \tag{3.34}$$

where

$$G(R) = R^6 - 6R^5 + 3d^2R^4 + 22d^2R^3 + 16d^4. \tag{3.35}$$

These results mean that the monotonicity of angular momentum and energy for a circular orbit switches at the points where $G = 0$. We find that, at least in the region far enough from the center $R \gg d$, the angular momentum $L_0(\rho, 0)$ and the energy $E_0(\rho, 0)$ are real positive values and monotonically increasing with R. We also derive h_0 evaluated at $z = 0$

$$h_0(\rho, 0) = \frac{16(R^2 - 3d^2)G}{R^2(R+2)^6F^2}. \tag{3.36}$$

If F vanishes, this quantity diverges, which is similar to the behaviors seen in $L_0(\rho, 0)$ and $E_0(\rho, 0)$. On the other hand, the Hessian $h_0(\rho, 0)$ vanishes at $R = \sqrt{3}d$ (i.e., $\rho = \sqrt{2}d$), where $z = 0$ and $\rho = \rho_0$ intersect each other. In addition, $h_0(\rho, 0)$ also vanishes for $G = 0$, which is similar to the behavior seen in Eqs. (3.33) and (3.34). This fact implies that the monotonicity of angular momentum and energy for a circular orbit switches at zeros of $h_0(\rho, 0)$. Taking into account $h_0(\rho, 0) > 0$ for $R \gg d$, we find that both angular momentum and energy monotonically increase with R on the sequence of stable circular orbits and monotonically decrease with R on the sequence of unstable circular orbits.

We discuss the dependence of the positions of stable circular orbits on the separation parameter d. Using the functions defined in the previous section, we plot the sequence of stable circular orbits as illustrated in Figs. 3.1. On the basis of these plots, dividing the range of d into five parts, we clarify the behavior of stable circular orbits for each range of d in the following subsections. Furthermore, we find the four critical values of d characterized by the behaviors of the sequence of stable circular orbits and the angular momentum of a circular orbit.

A $d > 1.401\cdots$

We focus on stable circular orbits in the case where the separation between the dihole is large enough (i.e., $d \gg 1$). Figure 3.1(a) shows a typical shape of the sequence of stable circular orbits for a large value of d. As seen from the figure, stable circular orbits exist on the line $z = 0$ in the range $\rho \in (\sqrt{2}d, \infty)$. The end point $(\rho, z) = (\sqrt{2}d, 0)$ is an MSCO because the sequence switches to that of unstable circular orbits at this point, where $h_0 = 0$. In addition, at this point the sequence of stable circular orbits bifurcates into the curve $\rho = \rho_0$, where ρ_0 is defined by Eq. (3.28). Finally it terminates near each black hole, which also correspond to MSCOs, especially the ISCOs.

Even in the sequence on $\rho = \rho_0$, the energy and the angular momentum of stable circular orbits monotonically decrease as the radius decreases up to the ISCOs. Note that, when d is large enough, a particle moving near each black holes feels gravity of a single black hole. Indeed, in the limit as $d \to \infty$, the ISCO radius measured by ρ approaches 3, which coincides with the ISCO radius of the single extremal Reissner–Nordström black hole spacetime.

As the value of d decreases from a large value, the ISCOs approach the intersection of $z = 0$ line and $\rho = \rho_0$ line. When the value of d reaches $1.401\cdots$, the three MSCOs merge at a point on $z = 0$ [see Fig. 3.1(b)]. As a result, the sequence of stable circular orbits only appears on the line $z = 0$.

B $d = d_0 = 1.401\cdots$

We find the critical value $d = d_0$ at which the three MSCOs degenerate [see Fig. 3.1(b)]. We expand ρ_0 in Eq. (3.28) around $z = 0$ up to $O(z^2)$,

$$\rho_0 = \sqrt{2}d - \frac{7}{9\sqrt{2}d}z^2 + O(z^4). \tag{3.37}$$

Substituting this expression into h_0, we expand it around $z = 0$ again,

$$h_0(\rho_0, z) = \frac{768\left(54d^2 - 33\sqrt{3}d - 26\right)}{d^2\left(9d - 2\sqrt{3}\right)^2\left(3d + 2\sqrt{3}\right)^6}z^2 + O(z^4). \tag{3.38}$$

As already discussed above, these results imply that there exists an MSCO at the point $(\rho, z) = (\sqrt{2}d, 0)$. Furthermore, since the condition of the multiple root is $\mathrm{d}^2h_0(\rho_0, z)/\mathrm{d}z^2 = O(z^2)$, i.e., $54d^2 - 33\sqrt{3}d - 26 = 0$, we obtain the critical value d_0 as

$$d_0 = \frac{11 + \sqrt{329}}{12\sqrt{3}} = 1.401\cdots. \tag{3.39}$$

Thus, in the case $d = d_0$, we find stable circular orbits on $z = 0$ plane in the range $\rho \in (\sqrt{2}d_0, \infty)$ and the ISCO at $(\rho, z) = (\sqrt{2}d_0, 0)$.

C $d_0 > d > 0.9713\cdots$

If we make d smaller than d_0, the sequence of stable circular orbits still appears only on $z = 0$ plane in the range $\rho \in (\sqrt{2}d, \infty)$ [see Fig. 3.1(c)], so that it is sufficient to analyze circular orbits on it. The end point $(\rho, z) = (\sqrt{2}d, 0)$ corresponds to the unique MSCO, especially the ISCO. When the value of d reaches $0.9713\cdots$, the region D becomes marginally connected at the intersection point of the lines $z = 0$ and $h_0 = 0$ [see Fig. 3.1(d)]. This intersection point is not an MSCO because the sequence of stable circular orbits does not switch to that of unstable circular orbits here. As a result, there exists the unique MSCO in the range $d_0 \geq d \geq 0.9713\cdots$.

D $d = d_* = 0.9713\cdots$

We seek the exact critical value $d = d_*$ at which the region D is marginally connected at the intersection point of the lines $z = 0$ and $h_0 = 0$ [see Fig. 3.1(d)]. In other words, the function h_0 has a saddle point at this point. We use this condition to derive d_* in what follows. From the explicit form of $h_0(\rho, 0)$ given in Eq. (3.36), we find that the condition $h_0(\rho, 0) = 0$ holds at $(R, z) = (\sqrt{3}d, 0)$, but the Hessian h_0 does not have a stationary point there. Therefore, we focus on the other branch

$$G = 0, \tag{3.40}$$

where G is defined by Eq. (3.35). A point satisfying this equation can be a stationary point of h_0 if $\mathrm{d}h_0(\rho, 0)/\mathrm{d}R = 0$, which reduces to

$$R^3 - 5R^2 + 2d^2R + 11d^2 = 0, \tag{3.41}$$

where we have used Eq. (3.40). Solving Eqs. (3.40) and (3.41) for d and R simultaneously, then we obtain the solutions

$$d_* = \frac{50(7 + \sqrt{129})}{(13 + \sqrt{129})\sqrt{710 + 70\sqrt{129}}} = 0.9713\cdots, \tag{3.42}$$

$$R_* = \frac{-19 + 3\sqrt{129}}{4} = 3.768\cdots. \tag{3.43}$$

The value of ρ corresponding to these solutions is given by

$$\rho_* = \frac{5}{512}(20291 - 1667\sqrt{129}) = 3.641\cdots. \tag{3.44}$$

The inverse of d_* coincides with the critical values M_* mentioned in Ref. [41]. Note that the linear stability of a circularly orbiting particle at $(\rho, z) = (\rho_*, 0)$ is undetermined, but the analysis of the allowed region of the particle motion shows it nonlinearly stable.

E $d_* > d > 0.5433\cdots$

If we make d smaller than d_*, the region D is separated into two regions [see Fig. 3.1(e)], and then two sequences of stable circular orbits appear on the line $z = 0$. The outer sequence appears from infinity to an MSCO, while the inner

sequence appears between another MSCO and the ISCO. Therefore, three MSCOs appear in total as the boundaries of these sequences. Their radii except for the ISCO radius are given as real roots for Eq. (3.40), and the ISCO radius is $\rho = \sqrt{2}d$.

As the value of d gradually decreases, the two sequences tend to separate from each other. In addition, the energy at the MSCO next to the ISCO increases. Remarkably, it reaches the energy level of a rest particle at infinity (i.e., $E = 1$) at $d = 0.7567\cdots$. Hence, for $d \leq 0.7567\cdots$, stable circular orbits with $E_0 \geq 1$ exist until the inner sequence disappears. Note that we do not observe such a phenomenon in the Kerr spacetime. Since circular orbits with $E_0 \leq 1$ occur more naturally, the sequence with $E_0 > 1$ does not contribute to phenomena such as accretion disk formation around the dihole.

Also, in this parameter range of d, an interesting feature arises. As the value of d decreases, the radius of the MSCO located next to the ISCO approaches the radius of the circular photon orbit, and eventually, the MSCO radius can be arbitrary close to the radius of the circular photon orbit. As a result, the angular frequency of a timelike particle on the MSCO can be comparable with that of the circular photon orbit. This feature does not appear in a single black hole case. Furthermore, it is known that the frequency of the circular photon orbit relates to the frequency of the quasinormal mode [76]. Thus, in the MP dihole spacetime, resonant excitation of a quasinormal mode that is a characteristic mode of the MP dihole spacetime may be happened by a timelike particle.

When the value of d reaches $0.5433\cdots$, the MSCO next to the ISCO is no longer a circular orbit because infinitely large angular momentum and energy are required to keep it a circular orbit [see Fig. 3.1(f)]. In the following subsection, we find the critical value of d from the behavior of L_0^2.

F $d = d_\infty = 0.5433\cdots$

As mentioned in the previous subsection, one of the three MSCOs located next to the ISCO disappears in the limit as $d \searrow 0.5433\cdots$. If a timelike particle circularly orbited at this limiting radius for $d = 0.5433\cdots$, the angular momentum L_0^2 would diverge. Therefore, to find the exact critical value d_∞, we analyze the behavior of $L_0^2(\rho, 0)$, which is given by Eq. (3.30). Notice that this expression and

Eq. (3.36) diverge if the following condition is satisfied:

$$F = 0. \tag{3.45}$$

It is worth pointing out that this condition is equivalent to that of the existence of circular photon orbits (see Appendix A). Since $F(R)$ has a local minimum at $R = 4/3$ and its extreme value takes the form $F(4/3) = 4(d^2 - 8/27)$, we find that the divergence of L_0^2 appears only at $\rho = \rho_\infty$ for $d = d_\infty$, where

$$d_\infty = \frac{2\sqrt{6}}{9} = 0.5433\cdots, \tag{3.46}$$

$$\rho_\infty = \frac{2\sqrt{30}}{9} = 1.217\cdots, \tag{3.47}$$

where ρ_∞ corresponds to $R = 4/3$. At $d = d_\infty$, hence the inner sequence of stable circular orbits on $z = 0$ plane exist in the range $\rho \in (\sqrt{2}d_\infty, \rho_\infty)$. The inverse of d_∞ coincides with $\bar{M}$ mentioned in Ref. [41].

For $d > d_\infty$, the angular momentum $L_0^2(\rho, 0)$ is positive and finite everywhere. This means that there exist stable/unstable circular orbits with arbitrary radii on $z = 0$ plane. On the other hand, for $d \leq d_\infty$, there exists no circular orbit of a massive particle on $z = 0$ plane in the range $\rho_{\rm ps} \leq \rho \leq \rho_{\rm pu}$ because L_0^2 can be negative or infinitely large there, where $\rho_{\rm ps}$ and $\rho_{\rm pu}$ are defined in Eqs. (A.4) and (A.5).

G $d_\infty > d > 0.3849\cdots$

If we make d smaller than d_∞, there still exist the two sequences of stable circular orbits on $z = 0$ plane [see Fig. 3.1(g)]. The outer sequence exists from infinity to an MSCO. The inner sequence exists in the range $\rho \in (\sqrt{2}d, \rho_{\rm ps})$, where $\rho = \sqrt{2}d$ is the ISCO radius and $\rho = \rho_{\rm ps}$ is the radius of the stable circular photon orbit, defined by Eq. (A.5) in Appendix A. The ISCO radius is smaller than the radius of the stable circular photon orbit. Note that L_0^2 diverges in the limit as $\rho \to \rho_{\rm ps}$ on the inner sequence, which is consistent with the appearance of the stable circular photon orbit.

As the value of d approaches $0.3849\cdots$, the value $\rho_{\rm ps}$ approaches $\sqrt{2}d$. When $d = 0.3849\cdots$, the inner sequence disappears [see Fig. 3.1(h)].

H $d = d_{\rm c} = 0.3849\cdots$

We seek the exact critical value of $d = 0.3849\cdots$ at which the inner sequence of stable circular orbits just disappears. The value of L_0^2 at $(\rho, z) = (\sqrt{2}d, 0)$ is given by

$$L_0^2(\sqrt{2}d, 0) = \frac{8\,(d + 3d_{\rm c})^2}{3\sqrt{3}\,(d - d_{\rm c})}, \tag{3.48}$$

where

$$d_{\rm c} = \frac{2\sqrt{3}}{9} = 0.3849\cdots. \tag{3.49}$$

This result together with Eq. (3.36) means that, even if d arbitrarily approaches to $d_{\rm c}$ from above, the point $(\rho, z) = (\sqrt{2}d, 0)$ is necessarily an MSCO. If $d = d_{\rm c}$, then L_0^2 at $(\rho, z) = (\sqrt{2}d_{\rm c}, 0)$ diverges, so that the inner sequence of stable circular orbits disappears. Consequently, we can identify $d_{\rm c}$ with the numerical critical value $d = 0.3849\cdots$. Thus, the location of the ISCO changes discontinuously at $d = d_{\rm c}$. Note that, however, the circular photon orbit exists there.

I $d_{\rm c} > d \geq 0$

If we make d smaller than $d_{\rm c}$, the single sequence of stable circular orbits appears on $z = 0$ plane from infinity to the ISCO. As the value of d approaches 0, the ISCO radius monotonically increases. For $d = 0$, the MP dihole becomes the single extremal Reissner–Nordström black hole with mass equal to 2 in our units. Then, the sequence of stable circular orbits exists from infinity to the ISCO radius equal to three times its mass. Therefore, we find the ISCO at $\rho = 6$ as shown in Fig. 3.1(i). Note that $z = 0$ plane at $d = 0$ is no longer special because spherical symmetry is restored.

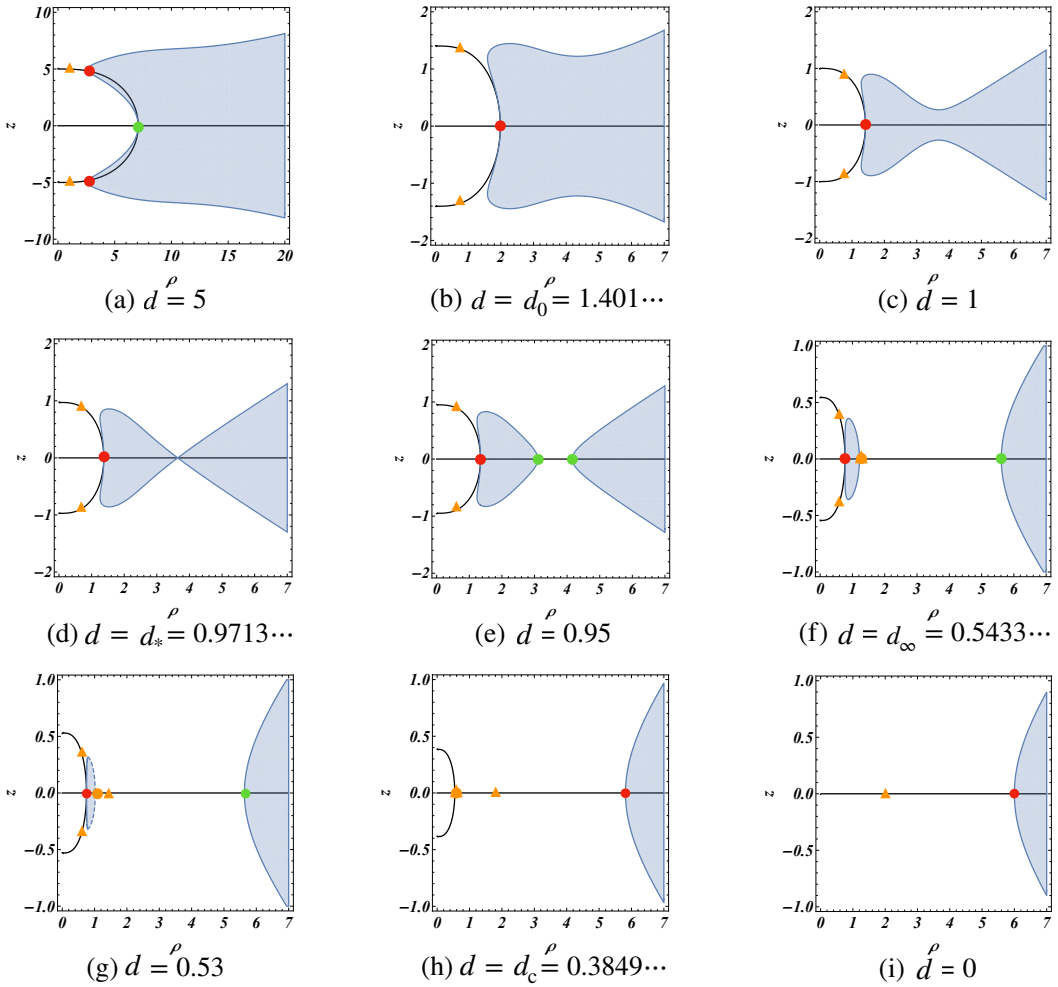

Figure 3.1: Positions of stable circular orbits of massive particles in ρ-z plane of the MP dihole spacetime with equal mass $M_+ = M_- = 1$ for the separation range $0 \leq d \leq 5$. The solid black lines represent the curves satisfying $U_z = 0$ (i.e., $z = 0$ and $\rho = \rho_0$). The shaded regions show the region D, where $h_0 > 0$, $k_0 > 0$, and $L_0^2 > 0$ are satisfied. The sequence of stable circular orbits is the solid black curves included in the region D. The solid blue lines are the boundary of D where $h_0 = 0$, $L_0^2 > 0$, and $k_0 > 0$. The dashed blue lines are the boundary of D where $h_0 > 0$, $k_0 > 0$, and L_0^2 diverges. The red dots are the positions of ISCOs. The green dots are the positions of marginally stable circular orbits (MSCOs) except for the ISCO. The orange triangles and dots are the positions of unstable circular photon orbits and stable ones, where L_0^2 diverges.

	separation	MSCOs	n(MSCOs)	ISCOs	n(ISCOs)
A.	$d > d_0 = 1.401\cdots$	(ρ_0, z) where $h_0(\rho_0, z) = 0$, $\lvert z\rvert \leq d$	3	(ρ_0, z) where $h_0(\rho_0, z) = 0$, $z \neq 0$	2
B.	$d = d_0$	$(\sqrt{2}d_0, 0)$	1	$(\sqrt{2}d_0, 0)$	1
C.	$d_0 > d > d_* = 0.9713\cdots$	$(\sqrt{2}d, 0)$	1	$(\sqrt{2}d, 0)$	1
D.	$d = d_*$	$(\sqrt{2}d_*, 0)$	1	$(\sqrt{2}d_*, 0)$	1
E.	$d_* > d > d_\infty = 0.5433\cdots$	$(\rho, 0)$ where $h_0(\rho, 0) = 0$	3	$(\sqrt{2}d, 0)$	1
F.	$d = d_\infty$	$(\rho, 0)$ where $h_0(\rho, 0) = 0$, $0 \leq L_0^2 < \infty$	2	$(\sqrt{2}d_\infty, 0)$	1
G.	$d_\infty > d > d_\mathrm{c} = 0.3849\cdots$	$(\rho, 0)$ where $h_0(\rho, 0) = 0$, $0 \leq L_0^2 < \infty$	2	$(\sqrt{2}d, 0)$	1
H.	$d = d_\mathrm{c}$	$(\rho, 0)$ where $h_0(\rho, 0) = 0$	1	$(\rho, 0)$ where $h_0(\rho, 0) = 0$	1
I.	$d_\mathrm{c} > d \geq 0$	$(\rho, 0)$ where $h_0(\rho, 0) = 0$	1	$(\rho, 0)$ where $h_0(\rho, 0) = 0$	1

Table 3.1: Positions in ρ-z plane and the numbers of the marginally stable circular orbits (MSCOs) and the innermost stable circular orbits (ISCOs) for each range of the separation parameter d. The item n(MSCOs) indicates the number of the MSCOs, and the item n(ISCOs) indicates the number of the ISCOs.

With the transition of the sequence of stable circular orbits, the numbers of MSCOs changes. We have summarized them in Table 3.1. The number of the MSCOs increases due to the bifurcation or the separation of the sequence. The radii of MSCOs and the ISCOs are plotted as a function of d in Fig. 3.2. The ISCO radius, shown by red lines, can be smaller than the ISCO radius in the single extremal Reissner–Nordström black hole spacetime. The location of the ISCO changes discontinuously at $d = d_{\rm c}$.

For an equal mass MP dihole with arbitrary separation, we have found stable circular orbits far from the dihole on the symmetric plane. These orbits balance by Newtonian gravitational force and centrifugal force. Near the dihole, however, stable circular orbits may balance by other mechanisms. As in the case of a familiar Schwarzschild black hole, a particle in the vicinity of the horizon feels the higher-order relativistic effect. On the other hand, since there is no horizon on the symmetric plane of this dihole spacetime, the centrifugal barrier of a particle inevitably diverges at the center. As a result, a radial stable equilibrium point appears by balancing the relativistic higher-order gravitational force and centrifugal force. Furthermore, if this point is also in a region bounded in the vertical direction, a stable circular orbit occurs. This mechanics is similar to that of the appearance of stable circular orbits near the 5D black ring [77, 78]. This suggests that the phenomenon occurs universally in the spacetime where there is no horizon at the center of the system.

We briefly mention unstable circular orbits for massive particles. For an arbitrary value of $d > 0$, there exists the sequence of unstable circular orbits on the symmetric plane in the range $\rho < \sqrt{2}d$, which are radially stable but vertically unstable. The sequence further appears between the pair of MSCOs on the symmetric plane for $d_\infty < d < d_*$ [see Fig. 3.1(e)], while it appears between the outermost MSCO and the unstable circular photon orbit for $0 \leq d \leq d_\infty$ [see Figs. 3.1(f)–3.1(i)]. In addition, we also find unstable circular orbits on $\rho = \rho_0$ for $d > d_{\rm c}$. They appear between the ISCO(s) and the unstable circular photon orbits. On these sequences, the energy and the angular momentum monotonically increase as the radius decreases.

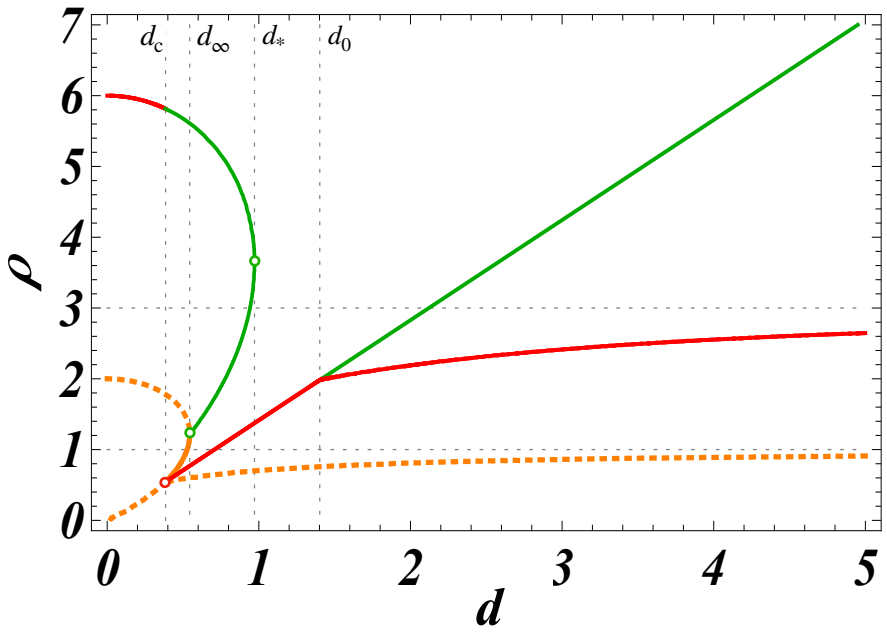

Figure 3.2: Dependence of the radii of marginally stable circular orbits and circular photon orbits on the separation parameter d in the Majumdar–Papapetrou dihole spacetime with equal unit mass. The green and red solid lines mark the radii of the marginally stable circular orbits (MSCOs) and innermost stable circular orbits (ISCOs), respectively. The orange dashed lines and the orange solid line are the unstable circular photon orbits and the stable circular photon orbits, respectively. For $d_c < d \leq d_\infty$, the radius of the ISCO is smaller than that of the stable circular photon orbit. At $d = d_c$, a discontinuous transition of ISCO position occurs.

3.3 Different mass case

In previous section, for the equal mass MP dihole spacetime, we have divided the range of the separation parameter d into five parts based on qualitative differences of the sequence of stable circular orbits and simultaneously have determined the four critical values as the boundaries of the ranges: d_0, d_*, d_∞ and d_c. In this section, we show that this division depends on its mass ratio and the mass ratio range separates into four parts, and we find three critical values as the boundaries.

A $1 > \nu > \nu_\infty = 0.7698\cdots$

We consider sequences of stable circular orbits for various values of d in the MP dihole spacetime with mass ratio $\nu \simeq 1$ but $\nu \neq 1$. We show sequences of stable circular orbits for several values of d in the case $\nu = 0.9$ in Fig. 3.3. On the basis of these typical plots, we discuss some qualitative properties of stable circular orbits and critical values of d. Specific numerical values for critical values d_0, d_*, d_∞, and d_c in this subsection are those for $\nu = 0.9$.

For a large value of d, we have two sequences of stable circular orbits on both sides of the dihole [see Fig. 3.3(a)]. The sequence on the large black hole side exists from infinity to the ISCO near the large black hole. On the other hand, the sequence on the small black hole side is restricted within a finite region. The inner boundary near the small black hole corresponds to the ISCO, and the outer boundary to an MSCO. As the value of d approaches a critical value $d_0(= 2.111\cdots)$ from above, the MSCO and the ISCO on the small black hole side approach each other. At $d = d_0$, these merge into one, and then the sequence on the small black hole side just disappears [see Fig. 3.3(b)]. If d becomes smaller than d_0, the sequence on the small black hole side no longer exists. We can interpret this disappearance as a consequence of relativistic effects because the corresponding sequences in Euler's three-body system, which is governed by Newtonian gravity, always exist for arbitrary values of d.

In the range $d_0 \geq d > d_*(= 0.9252\cdots)$, there exists a sequence of stable circular orbits only on the large black hole side, which appears from infinity to the ISCO [see Fig. 3.3(c)]. At $d = d_*$, the boundary of the region D touches the curve $\rho = \rho_0$ [see Fig. 3.3(d)]. This implies that two sequences of stable circular orbits are marginally connected at a point.

In the range $d_* \geq d > d_c(= 0.4679\cdots)$, two sequences of stable circular orbits appear [see Figs. 3.3(d)–3.3(g)]. The outer sequence exists from infinity to the outermost MSCO. On the other hand, the behavior of the inner sequence divides this range of d into two parts. For $d_* \geq d > d_\infty(= 0.5198\cdots)$, the inner sequence exists between an MSCO and the ISCO. However, at $d = d_\infty$, the outer MSCO disappears because infinitely large energy and angular momentum would be required for a massive particle [see Fig. 3.3(f)]. In other words, a circular photon orbit appears there. For $d_\infty \geq d > d_c$, the inner sequence appears between the

stable circular photon orbit and the ISCO [see Fig. 3.3(g)]. At $d = d_{\rm c}$, the stable circular photon orbit and the ISCO merge into one, and then the inner sequence just disappears [see Fig. 3.3(h)]. In the range $d_{\rm c} \geq d \geq 0$, there only exists a sequence of stable circular orbits, which appears from infinity to the ISCO [see Fig. 3.3(i)].

Consequently, we divide the range of d into five parts on the basis of typical behaviors of the sequence of stable circular orbits and introduce four critical values of d as the boundaries of these ranges as we have done in the case $\nu = 1$. Note that, however, each meaning of critical values is slightly generalized from those of $\nu = 1$. Here, let us summarize how we define the four critical values:

(i) $d = d_0$: The sequence of stable circular orbits on the small black hole side disappears.

(ii) $d = d_*$: The sequence of stable circular orbits on the large black hole side is divided into two parts.

(iii) $d = d_\infty$: A stable circular photon orbit appears at the outer boundary of the inner sequence of stable circular orbits on the large black hole side.

(iv) $d = d_{\rm c}$: The inner sequence of stable circular orbits on the large black hole side disappears.

In the following, according to the difference in the appearance of these critical values, we classify the range of the mass ratio ν into four parts. In each range of ν, we discuss the behavior of the sequence of stable circular orbits depending on d. Figure 3.8(a) shows the dependence of the radii of the MSCOs, the ISCOs, and the circular photon orbits on d in the case $\nu = 0.9$. In the range $d_{\rm c} < d \leq d_\infty$, the radius of the ISCO (red solid line) is smaller than the one of the stable circular photon orbit (orange solid line in the middle of the three). In addition, the discontinuous transition of the position of the ISCO occurs at $d = d_{\rm c}$. These phenomena are also seen in the equal mass MP dihole spacetime [43].

B $\nu = \nu_\infty = 0.7698\cdots$

If we decrease the value of ν from $\nu = 1$, then at

$$\nu = \nu_\infty := \frac{4\sqrt{3}}{9} = 0.7698\cdots, \tag{3.50}$$

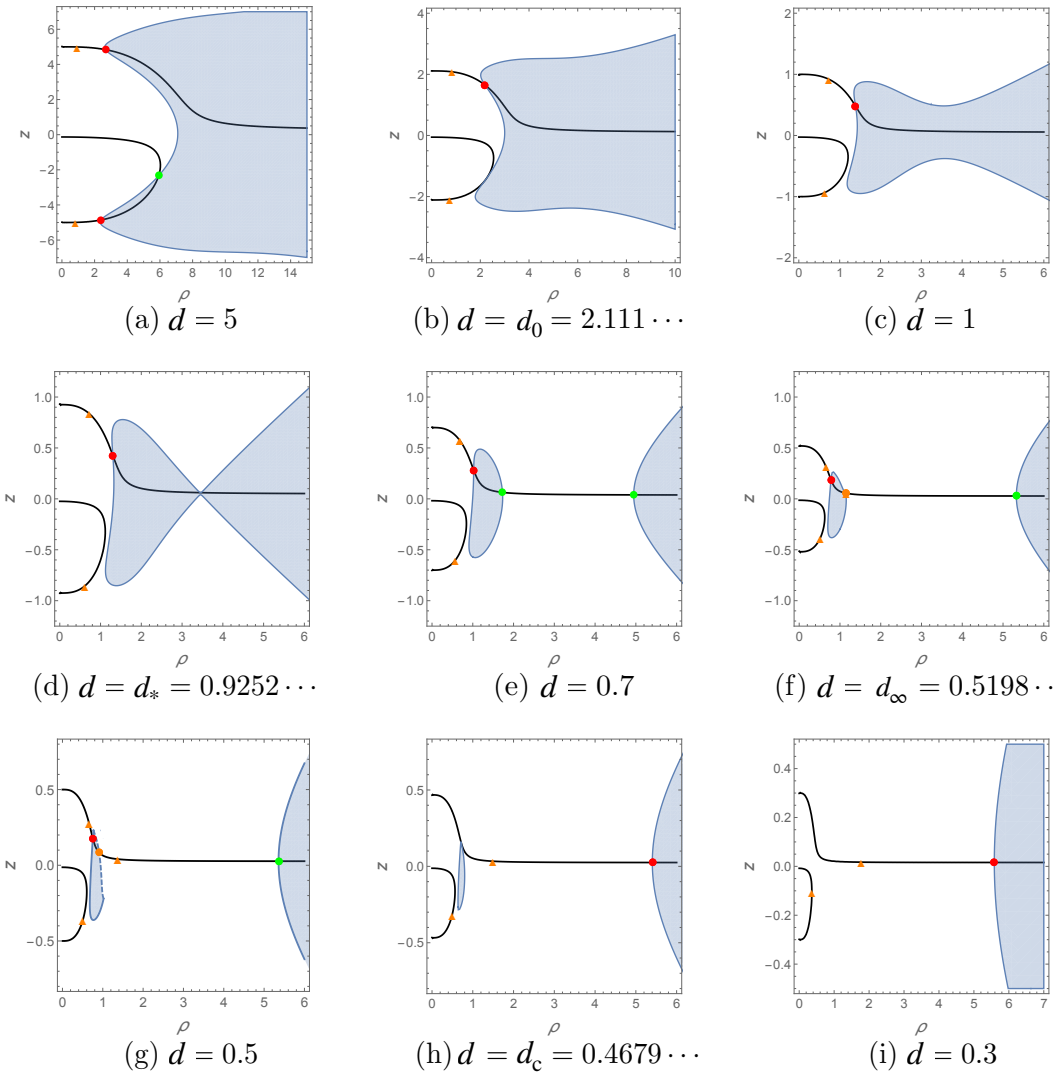

Figure 3.3: Sequences of stable circular orbits in the MP dihole spacetime with mass ratio $\nu = 0.9$. The green dots indicate the position of marginally stable circular orbits, and the red dots indicate the position of the innermost stable circular orbits. The orange dots show the positions of stable circular photon orbits, and the orange triangles show those of unstable ones.

the stable circular photon orbit no longer appears for any value of d. In other words, the critical value d_∞ disappears at $\nu = \nu_\infty$. We can interpret that the gravity of the small black hole is not sufficiently strong to make a photon orbit circular in the region far from the large black hole even if two black holes get close

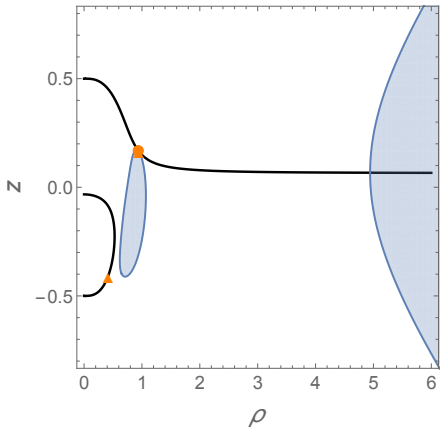

Figure 3.4: Sequences of stable circular orbits in the MP dihole spacetime with mass ratio $\nu = \nu_\infty = 0.7698\cdots$. The roles of each element in these plots are the same as those in Fig. 3.3.

each other. In what follows, we consider sequences of stable circular orbits in the case $\nu = \nu_\infty$.

For $d > 1/2$, the behavior of sequences of stable circular orbits is similar as that discussed in the previous subsection. Indeed, we find two critical values $d_0 = 2.269\cdots$ and $d_* = 0.8740\cdots$. We note that, however, qualitative differences from the case in the previous subsection appear at $d = 1/2$. In the limit as $d \searrow 1/2$, we find that the MSCO and the ISCO at the boundaries of the inner sequence merge into one at $(\rho, z) = (2\sqrt{2}/3, 1/6) = (0.9428\cdots, 0.1666\cdots)$ (see Fig. 3.4). Simultaneously, infinitely large energy and angular momentum are required for a massive particle to orbit circularly here. In other words, here is a stable/unstable circular photon orbit. These behaviors mean that d_c and d_∞ are degenerate at $d = 1/2$, that is, $d = d_c = d_\infty = 1/2$.

In the range $d < 1/2$, there is only a single sequence of stable circular orbits that appears from infinity to the ISCO, which is the same as that discussed in the previous section.

C $\nu_\infty > \nu > \nu_* = 0.5306\cdots$

We consider sequences of stable circular orbits for various values of d in the case where $\nu_\infty > \nu > \nu_* = 0.5306\cdots$. We can see typical sequences of stable circular orbits for $\nu = 0.7$ in Fig. 3.5. On the basis of these plots, we discuss the appearance of critical values d_0, d_*, and $d_{\rm c}$ in this range. Specific numerical values for these critical values in this subsection are those for $\nu = 0.7$.

For a relatively large value of d, a sequence of stable circular orbits appears from infinity to the ISCO on the large black hole side, while a sequence appears between an MSCO and the ISCO on the small black hole side [see Fig. 3.5(a)]. When d becomes smaller and smaller, at $d = d_0 (= 2.285\cdots)$, the sequence on the small black hole side disappears [see Fig. 3.5(b)]. When d becomes smaller and smaller yet, at $d = d_* (= 0.8520\cdots)$, the sequence on the large black hole side is divided into two parts. In the range $d_* \geq d > d_{\rm c} (= 0.6454\cdots)$, there are two sequences, the inner and the outer. As a result, we find three MSCOs as the boundaries of these sequences, and the innermost one corresponds to the ISCO. At $d = d_{\rm c}$, the inner sequence disappears. Note that the critical value d_∞ no longer exists in this range of ν. In the range $0 \leq d < d_{\rm c}$, we find a single sequence that appears from infinity to the ISCO. The dependence of the radii of the MSCOs, the ISCOs, and the circular photon orbits on d in the case $\nu = 0.7$ is shown in Fig. 3.8(b). The parameter range of d is divided by d_0, d_*, and $d_{\rm c}$ into four parts. The discontinuous transition of the ISCO on the large black hole side still occurs at $d = d_{\rm c}$. For any value of d, stable circular photon orbits do not exist.

D $\nu = \nu_* = 0.5306\cdots$

We focus on sequences of stable circular orbits for various values of d in the case $\nu = \nu_* = 0.5306\cdots$. For large d, we can see similar behavior of the sequences of stable circular orbits as is shown in the previous subsection. Indeed, we obtain the critical value $d_0 = 2.189\cdots$. We should note that the inner sequence of stable circular orbits appearing at $(\rho, z) = (2.279\cdots, 0.3637\cdots)$ for $d = d_* = 0.8327\cdots$ disappears as soon as it appears [see Fig. 3.6(d)]. This means that the critical values d_* and $d_{\rm c}$ are degenerate. Consequently, we have no inner sequence of stable circular orbits on the large black hole side.

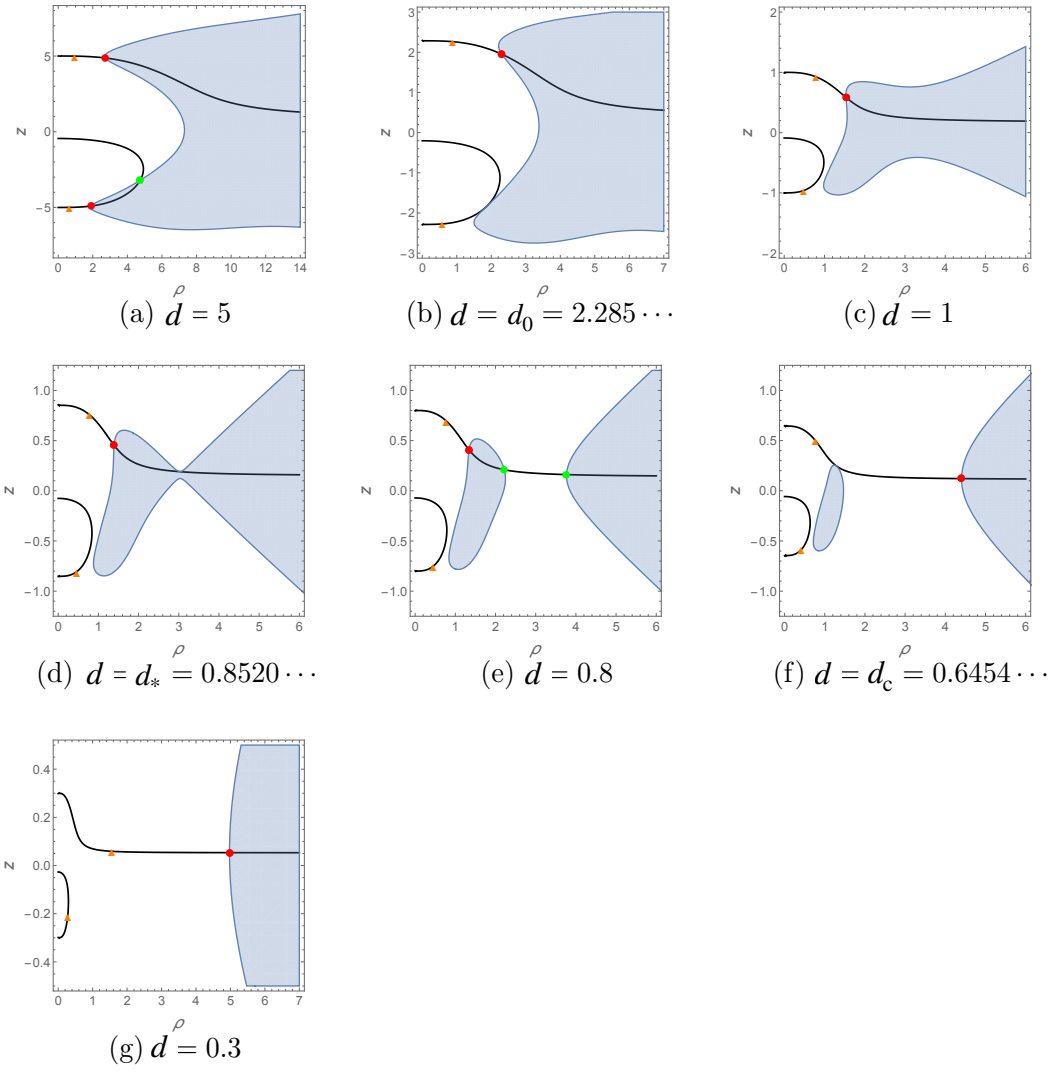

Figure 3.5: Sequence of stable circular orbits in the MP dihole spacetime with mass ratio $\nu = 0.7$. The roles of each element in these plots are the same as those in Fig. 3.3.

E $\nu_* > \nu > \nu_0 = 0.0110134\cdots$

Let us consider sequences of stable circular orbits for various values of d in the case where $0 < \nu < \nu_*$. Observing typical sequences for $\nu = 0.3$ in Fig. 3.7, we discuss the appearance of the critical value d_0 in this range. The specific numerical value of d_0 in this subsection is that for $\nu = 0.3$.

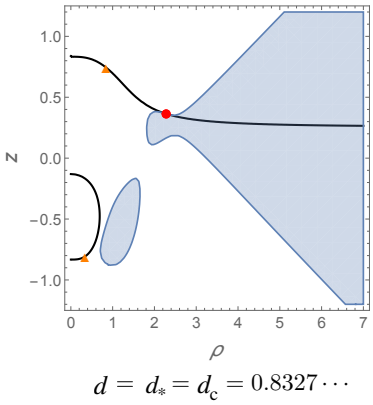

Figure 3.6: Sequences of stable circular orbits in the MP dihole spacetime with mass ratio $\nu = \nu_* = 0.5306\cdots$. The roles of each element in this plot are the same as those in Fig. 3.3.

For a large value of d, we find two sequences of stable circular orbits on both sides of the dihole [see Fig. 3.7(a)]. On the large black hole side, the sequence appears from infinity to the ISCO. On the small black hole side, the sequence appears from the outer MSCO to the ISCO. If d becomes smaller and reaches $d = d_0 (= 1.762\cdots)$, the sequence on the small black hole side disappears. Therefore, there still exists the critical value d_0 [see Fig. 3.7(b)]. In the range $d < d_0$, however, any qualitative change of the sequence of stable circular orbits does not occur on the large black hole side. The dependence of the radii of the MSCOs, the ISCOs, and the circular photon orbits on d in the case $\nu = 0.3$ is shown in Fig. 3.8(c). The parameter range of d is divided by d_0 into two parts. The discontinuous transition of the position of the ISCO on the large black hole side no longer occurs because there are no separated sequences of stable circular orbits on the large black hole side.

F $0 \leq \nu \leq \nu_0$

We mention the sequence of stable circular orbits in the range $0 \leq \nu \leq \nu_0$. When the value of ν reaches ν_0 from above, the critical value d_0 is equal to zero. This means that the sequence on the small black hole side does not vanish unless the two black holes coalesce into one. If we make the value of ν smaller than ν_0, any critical values of d do not appear. According to Fig. 3.8(d), where we set

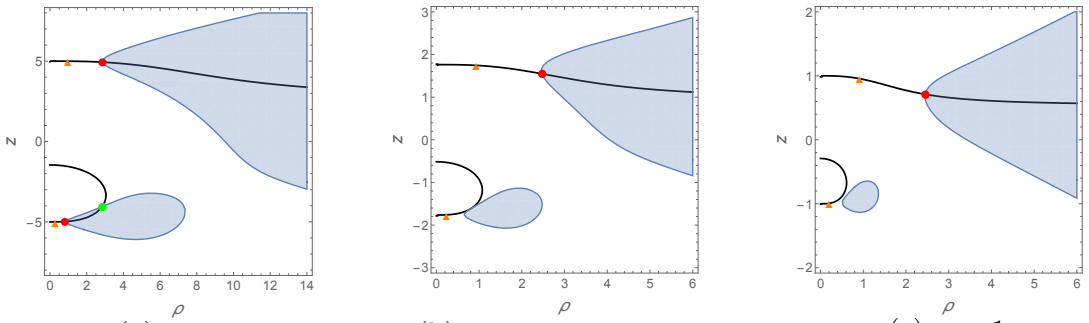

(a) $d = 5$ (b) $d = d_0 = 1.762\cdots$ (c) $d = 1$

Figure 3.7: Sequence of stable circular orbits in the MP dihole spacetime with mass ratio $\nu = 0.3$. The roles of each element in these plots are the same as those in Fig. 3.3.

$\nu = 0.01$, for $d > 0$, both the large and the small black holes have the sequence of the stable circular orbits; i.e., two MSCOs—one of these is also the ISCO—always appear on the small black hole.

Let us summarize the behaviors of stable circular orbits in the different mass MP dihole spacetime. When $\nu \simeq 1$ but $\nu \neq 1$, the sequence of the stable circular orbits changes as d varies in common with the case of $\nu = 1$, but we have generalized the definitions of the critical values of d to be valid for the case of the different mass MP dihole from those in the equal mass MP dihole spacetime [43]. When the value of d is relatively large, the sequence of stable circular orbits on the large black hole side exists from infinity to the ISCO while that on the small black hole side is restricted to a finite range. At $d = d_0$, the sequence on the small black hole side disappears. This phenomenon occurs due to the relativistic effect of the appearance of the ISCOs. Since the radius of the outer MSCO on the small black hole side decreases faster than the one of the ISCO as d decreases, the positions of the MSCO and the ISCO coincide with each other at $d = d_0$, and then the sequence on the small black hole side disappears [see the green and red dashed lines in Figs. 3.8(a)–3.8(c)]. For $d < d_0$, the sequence of stable circular orbits appears only on the large black hole side. When $d = d_*$, the sequence on the large black hole side is marginally connected at a point. In the range $d_c < d < d_*$, two sequences of the stable circular orbits appear on the large black hole side. The outer boundary of the inner sequence is an MSCO in $d_\infty < d < d_*$, while a stable

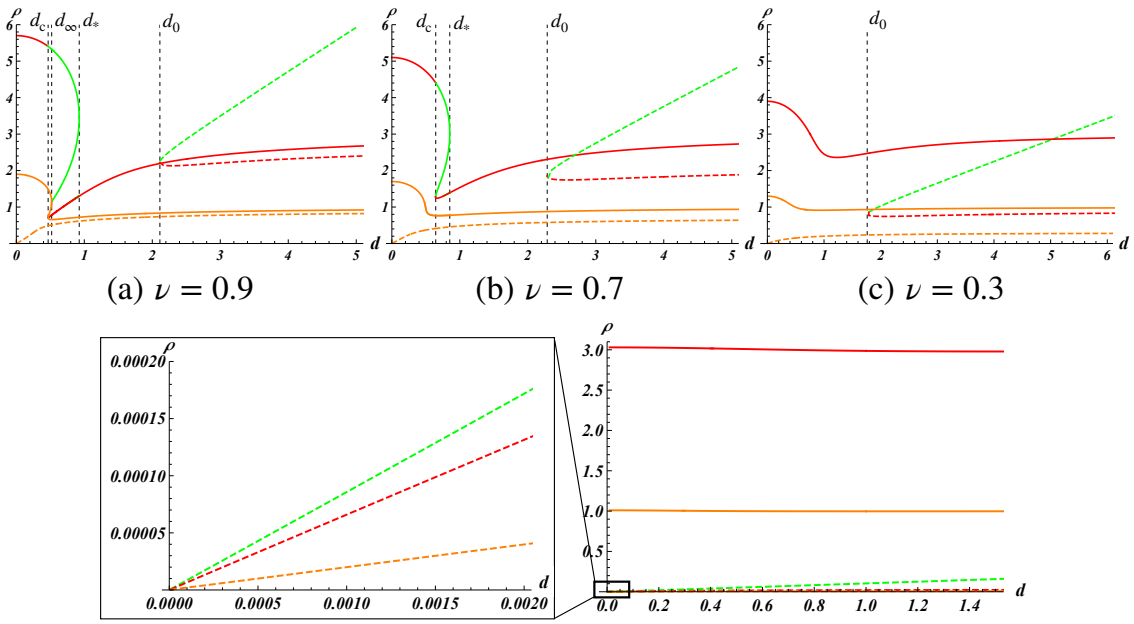

Figure 3.8: Dependence of the radii of MSCOs and circular photon orbits on the separation parameter d in the MP dihole spacetime with mass ratio: (a) $\nu = 0.9$, (b) $\nu = 0.7$, (c) $\nu = 0.3$, and (d) $\nu = 0.01$. The green and red solid lines show the radii of MSCOs on the large black hole side, and the green and red dashed lines show those on the small black hole side. In particular, the red lines indicate each ISCO. The orange solid lines show the radii of circular photon orbits on the large black hole side, and the orange dashed lines show those on the small black hole side. The dashed green and red lines merge at $d = d_0$ and then the sequence of the stable circular orbits on the small black hole side disappears. In cases (a) and (b), the green solid lines emerge at $d = d_*$, and the outer exist in the range $d_c < d < d_*$. In case (a), the inner exists in the range $d_\infty < d < d_*$, while in case (b), the one exists in the range $d_c < d < d_*$. In case (a), the stable circular photon orbits appear on the large black hole side in $d_c < d < d_\infty$ whereas they do not in the other cases. In case (d), the sequence on the small black hole side always exists because there is no critical value of d.

circular photon orbit in $d_c < d \leq d_\infty$. Finally, for $0 \leq d \leq d_c$, since the inner sequence vanishes, we have a single connected sequence from infinity to the ISCO

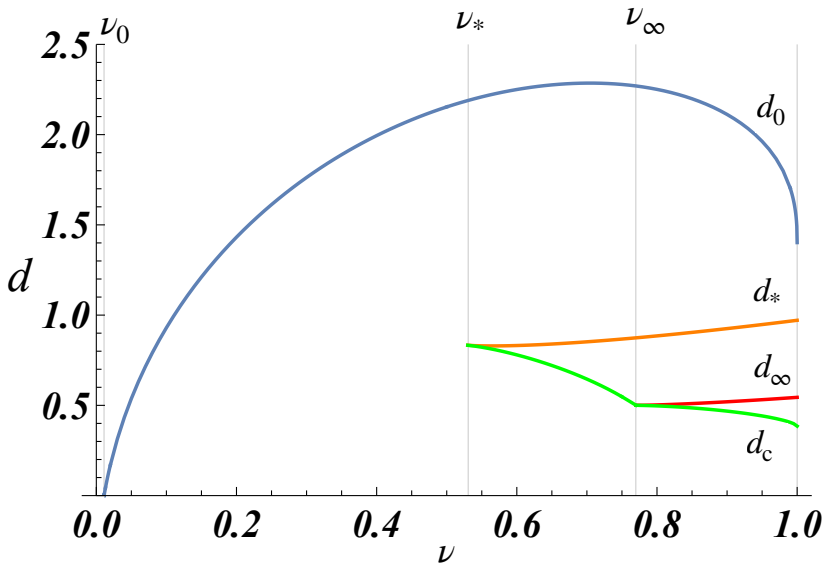

Figure 3.9: Dependence of critical values of the separation d on the mass ratio ν. The blue, orange, red, and green lines show $d = d_0$, d_*, d_∞, and d_c, respectively. The parameter range of ν is divided into four parts, and the appearance of the critical values changes drastically at the boundaries, $\nu = \nu_\infty$, ν_*, and ν_0. At $\nu = \nu_\infty$, the critical values d_∞ and d_c degenerate each other. At $\nu = \nu_*$, the critical values d_* and d_c coincide with each other. At $\nu = \nu_0$, the critical value d_0 disappears.

on the large black hole side.

We have also revealed the dependence of the sequence of stable circular orbits on ν. Figure 3.9 shows the relation between ν and the critical values of d. For $\nu > \nu_\infty = 0.7698\cdots$, the sequences of the stable circular orbits are qualitatively the same as these of the case $\nu \simeq 1$. At $\nu = \nu_\infty$, the two critical values d_∞ and d_c merge with each other, so that the parameter range of d is divided into four parts. At $\nu = \nu_* = 0.5306\cdots$, the critical values d_* and d_c coincide with each other. For $\nu < \nu_*$, the sequence on the large black hole side does not separate into two parts. The remaining critical value d_0 also disappears when $\nu = \nu_0 = 0.01101\cdots$. When we make the value of ν smaller than ν_0, the sequences of stable circular orbits on both sides do not vanish until the two black holes merge into one [see Fig. 3.8 (d)].

Chapter 4

Observability of the innermost stable circular orbit in a near-extremal Kerr black hole

The contents in this chapter originally published as:

T. Igata, K. Nakashi and K. Ogasawara, "Observability of the innermost stable circular orbit in a near-extremal Kerr black hole," Phys. Rev. D **101** (2020) no.4, 044044.

In this chapter, we investigate a photon escape probability from a light source on the innermost stable circular orbit (ISCO) in a (near-)extremal Kerr black hole. In particular, we show that in the extremal black hole, the escape probability of a photon approaches a nonzero value, even if the orbital radius of a light source is arbitrary close to the ISCO radius that coincides with the horizon radius. The analysis method we use in this chapter is applicable when the geometrical optics approximation is valid. This means the results are applicable when the wavelength of electromagnetic waves emitted from a light source is sufficiently less than the gravitational radius of a black hole. We do not consider the effect of a light polarization.

4.1 Avoidance cone in the Schwarzschild black hole

In this section, we discuss an avoidance cone in the Schwarzschild black hole. The null geodesics emitted to the inside of the avoidance cone must fall into the black hole. Thus, the null geodesics emitted to the outside of it can escape to the infinity. The discussion is based on [79].

We assume that a light source emits photons isotropically and is being at rest with respect to the event horizon of the Schwarzschild spacetime. We consider the null geodesics in the equatorial plane because the background spacetime possesses spherical symmetry. With this assumptions, we can parameterize the spatial part of a geodesic by the angular coordinate ϕ: $\mathbf{x} = \mathbf{x}(\phi)$. The unit tangent three vector $\mathbf{e}$ to a null geodesic is given by

$$\mathbf{e} = \left[f(r)^{-1} \left(\frac{\mathrm{d}r}{\mathrm{d}\phi} \right) + r^2 \right]^{-1/2} \left(\frac{\mathrm{d}r}{\mathrm{d}\phi}, 0, 1 \right), \tag{4.1}$$

where $f(r) = 1 - 2/r$. We define the half-angle of the cone Ψ, which consists of a emitted null geodesic and the radial axis, as the inner product of the tangent vector $\mathbf{e}$ and the unit vector $\mathbf{e_r} = (\sqrt{f}, 0, 0)$:

$$\cos\Psi = (\mathbf{e}, \mathbf{e_r}) = \frac{\mathrm{d}r/\mathrm{d}\phi}{\sqrt{fr^2 + (\mathrm{d}r/\mathrm{d}\phi)^2}}. \tag{4.2}$$

From this expression, we have

$$\tan^2\Psi = f(r) r^2 \left(\frac{\mathrm{d}r}{\mathrm{d}\phi} \right)^{-2}. \tag{4.3}$$

Combining the geodesic equations, we obtain

$$\left(\frac{\mathrm{d}r}{\mathrm{d}\phi} \right)^2 = \frac{r^4}{b^2} - fr^2, \tag{4.4}$$

where $b = L/E$ is an impact parameter. The value of the impact parameter corresponding to the circular photon orbit is $b_{\mathrm{pc}} = 3\sqrt{3}$. Substituting this value and Eq. (4.4) into Eq. (4.3), we obtain the half-angle of the avoidance cone

$$\tan\Psi = \frac{\sqrt{r/2 - 1}}{(r/3 - 1)\sqrt{r/6 + 1}}. \tag{4.5}$$

From this equation, when $r \to \infty$, $\Psi \to 3\sqrt{3}/r$. For $r = 3$, that is the radius of the circular photon orbit, $\Psi = \pi/2$, while for $r = 2$, $\Psi = \pi$. Therefore, the amplitude of the avoidance cone increases as the radius of the source decreases. In terms of the escape cone, the amplitude of the escape cone decreases as the radius of the source decreases, and eventually, the escape cone disappears at the event horizon.

4.2 Escape probability of photon from vicinity of black hole horizon

4.2.1 Conditions for photon escaping

We review conditions for a photon escaping from the vicinity of the horizon to infinity [55]. To derive them, we analyze the null geodesic equation in radial direction (2.77), which is rewritten as

$$\dot{r}^2 + \frac{r(r-2)}{\Sigma^2}(b - b_1)(b - b_2) = 0, \tag{4.6}$$

where

$$b_1(r) = \frac{-2ar + [r\Delta(r^3 - qr + 2q)]^{1/2}}{r(r-2)}, \tag{4.7}$$

$$b_2(r) = \frac{-2ar - [r\Delta(r^3 - qr + 2q)]^{1/2}}{r(r-2)}. \tag{4.8}$$

We call b_i $(i = 1, 2)$ the effective potentials for photon's radial motion. The allowed parameter range of b for a positive energy photon is

$$b \leq b_1 \quad \text{for} \quad r_{\rm h} < r < 2, \tag{4.9}$$

$$b_2 \leq b \leq b_1 \quad \text{for} \quad r \geq 2. \tag{4.10}$$

Since the photon escaping is governed by the potential barrier, the extremum points of b_i $(i = 1, 2)$ should be clarified. Solving $\mathrm{d}b_i/\mathrm{d}r = 0$ for q, we obtain a common equation

$$q = \tilde{f}(r) \equiv \frac{r^2}{a^2}\left[-\frac{4(1-a^2)r}{(r-1)^2} + 3 + (3-r)(r-1)\right]. \tag{4.11}$$

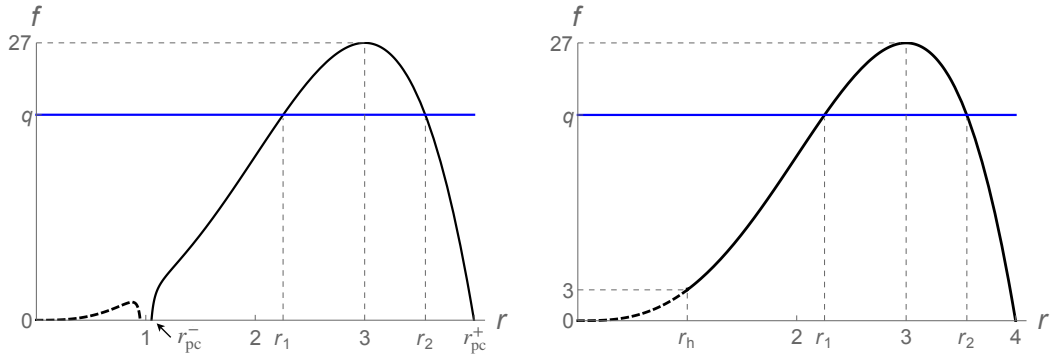

(a) $a = 0.999$ (b) $a = 1$

Figure 4.1: Relation between the impact parameter q and the radii r_i $(i = 1, 2)$ of extremum points of the effective potentials $b_i(r)$. The function $\tilde{f}$ is shown by black lines, which are solid outside the horizon and dashed inside it. The left panel (a) is a subextremal case ($a = 0.999$), and the right panel (b) is the extremal case ($a = 1$).

It is sufficient to investigate the region where $\tilde{f}(r) \geq 0$ because the light source we discuss is located on the equatorial plane, and therefore, from Eqs. (2.78) and (2.81), a photon must initially satisfy $\Theta = q \geq 0$.

First we consider the subextremal Kerr spacetime: $0 < a < 1$. Figure 4.1(a) shows a typical shape of $\tilde{f}(r)$ in this case. This figure shows that Eq. (4.11) has two roots r_1, r_2 outside the horizon, which are restricted in the range

$$r_{\rm h} < r_{\rm pc}^- \leq r_1 \leq 3 \leq r_2 \leq r_{\rm pc}^+, \tag{4.12}$$

where $r = 3$ is a local maximum point of $\tilde{f}$, and $r_{\rm pc}^\pm$ are radii of circular photon orbits given by Eq. (2.41). When a photon stays at the top of an extremum point of b_1 (b_2), the orbit with constant radius $r = r_1$ ($r = r_2$) is called the spherical photon orbit. Then, the photon must have

$$b = b_i^{\rm s} \equiv \frac{2(1-a^2)}{a(r_i - 1)} - \frac{(r_i - 1)^2}{a} + \frac{3}{a} - a. \tag{4.13}$$

Next, we focus on the case of the extremal Kerr spacetime: $a = 1$, for which the first term in the square brackets of Eq. (4.11) vanishes. Therefore, Eq. (4.11) reduces to

$$q = r^3(4 - r). \tag{4.14}$$

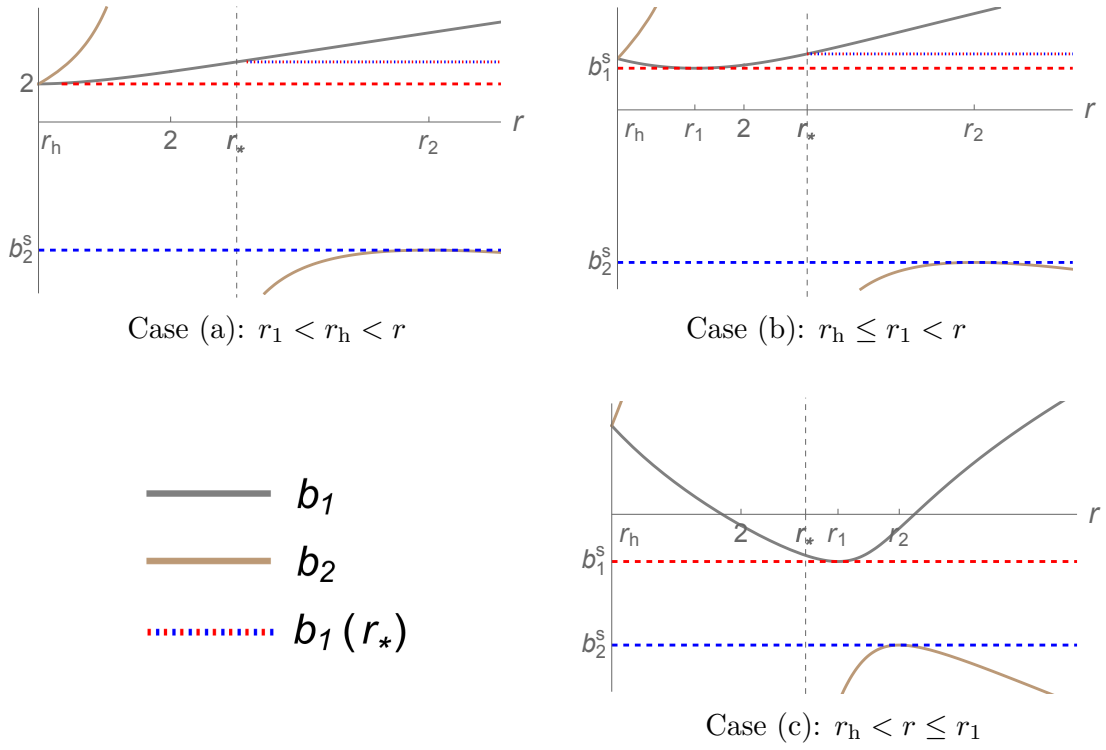

Figure 4.2: Typical shapes of the effective potentials b_i $(i = 1, 2)$ and parameter ranges of b for escaping photons. The radius r_* indicates the radial position of the source.

Figure 4.1(b) shows the shape of $\tilde{f}$ in the extremal case. In contrast to the subextremal case, the number of roots of Eq. (4.11) depends on q. Outside the horizon, there exists a single root r_2 for $0 \le q \le 3$, while there exist two roots r_1, r_2 outside the horizon for $3 < q < 27$, where the boundary values of the ranges come from $\tilde{f}(r_h) = 3$ and $\tilde{f}(3) = 27$.

Let us consider escape conditions for a photon in terms of (b, q). Classifying the radial position r of a light source based on relations with the extremum point r_1 and the horizon r_h, we clarify the parameter range of (b, q) for a photon that can escape from the vicinity of the horizon to infinity. We also determine the marginal pairs of (σ_r, b) for a photon that cannot marginally escape. In the following part, it is assumed that $r < 3$.

Case a.—We consider the case $r_1 < r_h < r$, which we define as Case a. Note that this inequality appears only for the extremal case because $r_1 > r_h$ always

holds for the subextremal case [see Fig. 4.1 and Eq. (4.12)]. The first inequality $r_1 < r_{\rm h}$ leads to $0 \leq q < 3$. In this range of q, we have typical plots of b_1, b_2 and marginal parameter values of b, as shown in Fig. 4.2(a). From this plot, the allowed range of b for a photon escaping can be read as follows: if $\sigma_r = +$ (i.e., radially outward emission), a photon with $b_2^{\rm s} < b \leq b_1$ (i.e., the bounded range between the blue lines) can escape to infinity. Even if $\sigma_r = -$ (i.e., radially inward emission), a photon with $2 < b < b_1$ (i.e., the bounded range between the red lines) can do so. Hence, we find that the marginal parameter values of b are given by $(\sigma_r, b) = (+, b_2^{\rm s}),\ (-, 2)$.

Case b.—We consider the case $r_{\rm h} \leq r_1 < r$, which we define as Case b. The corresponding range of q is $3 \leq q < \tilde{f}$ for $a = 1$ and $0 \leq q < \tilde{f}$ for $0 < a < 1$. Figure 4.2(b) shows typical plots of b_i in these ranges of q. If $\sigma_r = +$, a photon with $b_2^{\rm s} < b \leq b_1$ (i.e., between the blue lines) can escape infinity, while if $\sigma_r = -$, a photon with $b_1^{\rm s} < b < b_1$ (i.e., between the red lines) can do so. Hence, we find that marginal parameter values of b are given by $(\sigma_r, b) = (+, b_2^{\rm s}), (-, b_1^{\rm s})$.

Case c.—We consider the case $r_{\rm h} < r \leq r_1$, which we define as Case c. Then, the parameter range of q is restricted to $\tilde{f} \leq q < 27$. Figure 4.2(c) shows typical plots of b_i in this ranges. Only if $\sigma_r = +$, a photon can escape to infinity, and it must then have $b_2^{\rm s} < b < b_1^{\rm s}$ (i.e., between the red and blue lines). Hence, we find that marginal parameter values b are given by $(\sigma_r, b) = (+, b_1^{\rm s}), (+, b_2^{\rm s})$.

The allowed parameter values of (b, q) for escape from the vicinity of the horizon are summarized in Tables 4.1 and 4.2.

Cases	q	b $(\sigma_r = +)$	b $(\sigma_r = -)$	Marginal pairs of (σ_r, b)
(a) $r_1 < r_{\rm h} < r$	$0 \leq q < 3$	$b_2^{\rm s} < b \leq b_1$	$2 < b < b_1$	$(+, b_2^{\rm s})$ and $(-, 2)$
(b) $r_{\rm h} \leq r_1 < r$	$3 \leq q < \tilde{f}$	$b_2^{\rm s} < b \leq b_1$	$b_1^{\rm s} < b < b_1$	$(+, b_2^{\rm s})$ and $(-, b_1^{\rm s})$
(c) $r_{\rm h} < r \leq r_1$	$\tilde{f} \leq q < 27$	$b_2^{\rm s} < b < b_1^{\rm s}$	n/a	$(+, b_2^{\rm s})$ and $(+, b_1^{\rm s})$

Table 4.1: $(a = 1)$ Allowed parameter values of (b, q) for escape from the vicinity of the horizon in the extremal Kerr spacetime.

Cases	q	b $(\sigma_r = +)$	b $(\sigma_r = -)$	Marginal pairs of (σ_r, b)
(b) $r_{\rm h} \leq r_1 < r$	$0 \leq q < \tilde{f}$	$b_2^{\rm s} < b \leq b_1$	$b_1^{\rm s} < b < b_1$	$(+, b_2^{\rm s})$ and $(-, b_1^{\rm s})$
(c) $r_{\rm h} < r \leq r_1$	$\tilde{f} \leq q < 27$	$b_2^{\rm s} < b < b_1^{\rm s}$	n/a	$(+, b_2^{\rm s})$ and $(+, b_1^{\rm s})$

Table 4.2: $(0 < a < 1)$ Allowed parameter values of (b, q) for escape from the vicinity of the horizon in a subextremal Kerr black hole spacetime.

4.2.2 Escape cone, escape probability, and redshift

We focus on a light source circularly orbiting a rotating black hole on the equatorial plane $\theta = \pi/2$. The energy E and angular momentum L of a source in a direct circular orbit of radius r are given by [65]

$$E = \frac{r^{3/2} - 2r^{1/2} + a}{r^{3/4}(r^{3/2} - 3r^{1/2} + 2a)^{1/2}}, \tag{4.15}$$

$$L = \frac{r^2 - 2ar^{1/2} + a^2}{r^{3/4}(r^{3/2} - 3r^{1/2} + 2a)^{1/2}}. \tag{4.16}$$

We restrict the orbital radius r of the source in the range $r \geq r_{\rm I}$, where $r_{\rm I}$ is the ISCO radius,

$$r_{\rm I} = 3 + Z_2 - \left[(3 - Z_1)(3 + Z_1 + 2Z_2)\right]^{1/2}, \tag{4.17}$$

$$Z_1 = 1 + (1 - a^2)^{1/3}\left[(1 + a)^{1/3} + (1 - a)^{1/3}\right], \tag{4.18}$$

$$Z_2 = (3a^2 + Z_1^2)^{1/2}. \tag{4.19}$$

Note that $r_{\rm I}$ approaches $r_{\rm h}$ as a approaches the extremal value 1. In the extremal case, $r_{\rm I}$ coincides with the horizon radius, i.e., $r_{\rm I} = r_{\rm h} = 1$ (see Fig. 2.2).

To describe a photon emission from the source, we introduce a frame $\{e^{(0)}, e^{(1)}, e^{(2)}, e^{(3)}\}$ associated with rest frame of the source,

$$e^{(0)} = -E{\rm d}t + L{\rm d}\varphi, \tag{4.20}$$

$$e^{(1)} = \frac{r}{\sqrt{\Delta}}{\rm d}r, \tag{4.21}$$

$$e^{(2)} = r{\rm d}\theta, \tag{4.22}$$

$$e^{(3)} = \frac{\sqrt{\Delta}}{r^{3/4}(r^{3/2} - 3r^{1/2} + 2a)^{1/2}}\left[(r^{3/2} + a){\rm d}\varphi - {\rm d}t\right], \tag{4.23}$$

which is a tetrad only on circular orbits of a timelike particle in the equatorial plane. We note that the direction of travel of a source is $e^{(3)}$ direction. Then, the

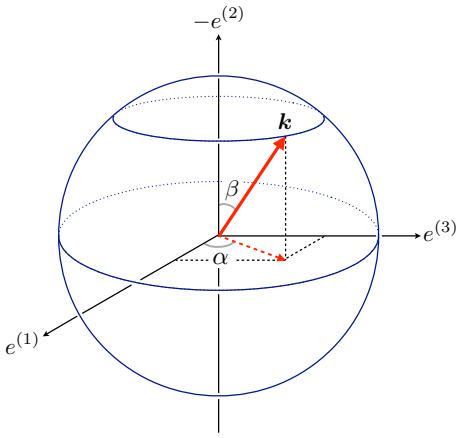

Figure 4.3: Definition of photon emission angles at a light source.

tetrad components of k^μ at the source position are $k^{(a)} = k^\mu e^{(a)}{}_\mu|_{\theta=\pi/2}$, where

$$k^{(0)} = \frac{b - a - r^{3/2}}{r^{3/4}(r^{3/2} - 3r^{1/2} + 2a)^{1/2}}, \tag{4.24}$$

$$k^{(1)} = \frac{\sigma_r}{r}\sqrt{\frac{R}{\Delta}}, \tag{4.25}$$

$$k^{(2)} = \sigma_\theta \frac{\sqrt{q}}{r}, \tag{4.26}$$

$$k^{(3)} = \frac{bE - L}{\sqrt{\Delta}}. \tag{4.27}$$

We parametrize the spatial direction of photon emission by two angle parameters (α, β) as follows:

$$\cos\alpha \sin\beta = \frac{k^{(1)}}{k^{(0)}}, \quad \cos\beta = -\frac{k^{(2)}}{k^{(0)}}, \quad \sin\alpha \sin\beta = \frac{k^{(3)}}{k^{(0)}}, \tag{4.28}$$

where β is the polar angle measured from the direction $-e^{(2)}$ to the direction of $\boldsymbol{k}$ (projection of k^μ normal to $e^{(0)}$), and α is the azimuthal angle measured from the direction $e^{(1)}$ to the projection of $\boldsymbol{k}$ on the plane spanned by $\{e^{(1)}, e^{(3)}\}$.[1]

[1]The angles α and β are related to the directional cosines Ψ and Θ of a beam of radiation with respect to ϕ-direction and θ-direction in Ref. [57] as

$$\Theta = \beta, \quad \cos\Psi = \sin\alpha \sin\beta. \tag{4.29}$$

Figure 4.3 shows the relation between $\boldsymbol{k}$ and (α, β). Solving these relations for (α, β) and using the null condition, we have

$$\cos\alpha = \frac{k^{(1)}}{\sqrt{(k^{(1)})^2 + (k^{(3)})^2}}, \quad \sin\alpha = \frac{k^{(3)}}{\sqrt{(k^{(1)})^2 + (k^{(3)})^2}}, \tag{4.30}$$

$$\cos\beta = -\frac{k^{(2)}}{k^{(0)}}, \qquad \sin\beta = \frac{\sqrt{(k^{(1)})^2 + (k^{(3)})^2}}{k^{(0)}}. \tag{4.31}$$

As a result, a pair (b, q) has a one-to-one relation to a pair of emission angles (α, β). Hence, the allowed parameter ranges of (b, q) for photon escape restrict the range of (α, β).

We now relate marginal parameter values for photon escape to (α, β). Let S be the complete set of emission angles (α, β) at which a photon can escape to infinity. We call S the escape cone of a photon. If a photon has emission angles of the boundary values of S, it cannot escape to infinity anymore. We call the set of all critical emission angles ∂S; this set can be explicitly specified in terms of marginal parameter values that determine given in Tables 4.1 and 4.2 as follows:

$$\partial S = \bigcup_{i=1,2} \left\{ (\alpha_i, \beta_i) \,\middle|\, 0 \le q \le 27 \right\}, \tag{4.32}$$

where, in the extremal case, we have defined

$$(\alpha_1, \beta_1) \equiv \begin{cases} (\alpha_{1(\mathrm{a})}, \beta_{1(\mathrm{a})}) \equiv (\alpha, \beta)\big|_{\substack{\sigma_r = - \\ b = 2}} & \text{for } 0 \le q < 3, \quad (4.33\mathrm{a}) \\ (\alpha_{1(\mathrm{b})}, \beta_{1(\mathrm{b})}) \equiv (\alpha, \beta)\big|_{\substack{\sigma_r = - \\ b = b_1^{\mathrm{s}}}} & \text{for } 3 \le q < \tilde{f}, \quad (4.33\mathrm{b}) \\ (\alpha_{1(\mathrm{c})}, \beta_{1(\mathrm{c})}) \equiv (\alpha, \beta)\big|_{\substack{\sigma_r = + \\ b = b_1^{\mathrm{s}}}} & \text{for } \tilde{f} \le q \le 27, \quad (4.33\mathrm{c}) \end{cases}$$

$$(\alpha_2, \beta_2) \equiv (\alpha, \beta)\big|_{\substack{\sigma_r = + \\ b = b_2^{\mathrm{s}}}} \quad \text{for} \quad 0 \le q \le 27, \tag{4.34}$$

and in a subextremal case,

$$(\alpha_1, \beta_1) \equiv \begin{cases} (\alpha_{1(\mathrm{b})}, \beta_{1(\mathrm{b})}) \equiv (\alpha, \beta)\big|_{\substack{\sigma_r = - \\ b = b_1^{\mathrm{s}}}} & \text{for } 0 \le q < \tilde{f}, \quad (4.35\mathrm{a}) \\ (\alpha_{1(\mathrm{c})}, \beta_{1(\mathrm{c})}) \equiv (\alpha, \beta)\big|_{\substack{\sigma_r = + \\ b = b_1^{\mathrm{s}}}} & \text{for } \tilde{f} \le q \le 27, \quad (4.35\mathrm{b}) \end{cases}$$

$$\big(\alpha_2,\beta_2\big)\equiv\big(\alpha,\beta\big)\big|_{\substack{\sigma_r=+\\ b=b_2^{\rm s}}}\quad\text{for}\quad 0\le q\le 27. \tag{4.36}$$

Figure 4.4 shows the critical emission angles for photon escape. The red, green, blue, and orange lines show the critical angles $(\alpha_{1(\rm a)},\beta_{1(\rm a)})$, $(\alpha_{1(\rm b)},\beta_{1(\rm b)})$, $(\alpha_{1(\rm c)},\beta_{1(\rm c)})$, and (α_2,β_2), respectively. Note that the region containing the coordinate origin bounded by critical angles corresponds to an escape cone. Figures 4.4(a)–4.4(c) show escape cones in the cases $r=2.98$, 2.6, $r_{\rm I}(=2.32\cdots)$, respectively, for $a=0.9$. The horizon radius is $r_{\rm h}\simeq 1.43\cdots$. The area of the escape cones becomes smaller as the light source position approaches the ISCO. Figures 4.4(d)–4.4(f) show escape cones in the cases $r=2.98$, 2, $r_{\rm I}(=1.18\cdots)$, respectively, for $a=0.999$. The horizon radius is $r_{\rm h}=1.04\cdots$. As in the case for $a=0.9$, the area of the escape cones becomes smaller as r approaches the ISCO radius. Comparing photon emissions from the ISCO, we can see that the area of the escape cone in the case of $a=0.999$ is smaller than that of $a=0.9$. Figures 4.4(g)–4.4(i) show escape cones in the cases $r=2.98, 2, 1.001$, respectively, for $a=1$. The area of the escape cones becomes smaller as r decreases. It must be noted that, according to Fig. 4.4(i), even if the radial coordinate value of an emission point is sufficiently close to the horizon, $r=1$, the escape cone still occupies over half of the unit sphere, indicating that more than half of the photons isotropically emitted from a circularly orbiting source can escape to infinity. In particular, as the entire region for which $0\le\alpha<\pi$ is included in the escape cone, all photons emitted forwardly from the source can escape to infinity.

We now assume that photon emission is isotropic and then evaluate the escape probability; this is identified with the solid angle of an escape cone divided by 4π:

$$P=\frac{1}{4\pi}\int_S {\rm d}\alpha{\rm d}\beta\sin\beta. \tag{4.37}$$

In subextremal cases, in terms of critical angles, the escape probability P can be written as

$$P=1-\frac{1}{2\pi}\int_{r_{\rm pc}^-}^{r}{\rm d}r_1\frac{{\rm d}\alpha_{1(\rm b)}}{{\rm d}r_1}\cos\beta_{1(\rm b)}-\frac{1}{2\pi}\int_{r}^{3}{\rm d}r_1\frac{{\rm d}\alpha_{1(\rm c)}}{{\rm d}r_1}\cos\beta_{1(\rm c)}-\frac{1}{2\pi}\int_{3}^{r_{\rm pc}^+}{\rm d}r_2\frac{{\rm d}\alpha_{2}}{{\rm d}r_2}\cos\beta_{2}. \tag{4.38}$$

We note that the light source position satisfies $r_{\rm pc}^-<r_{\rm I}\le r<3$, where the first equality $r_{\rm pc}^-<r_{\rm I}$ is always satisfied in the subextremal case. All the integrands in

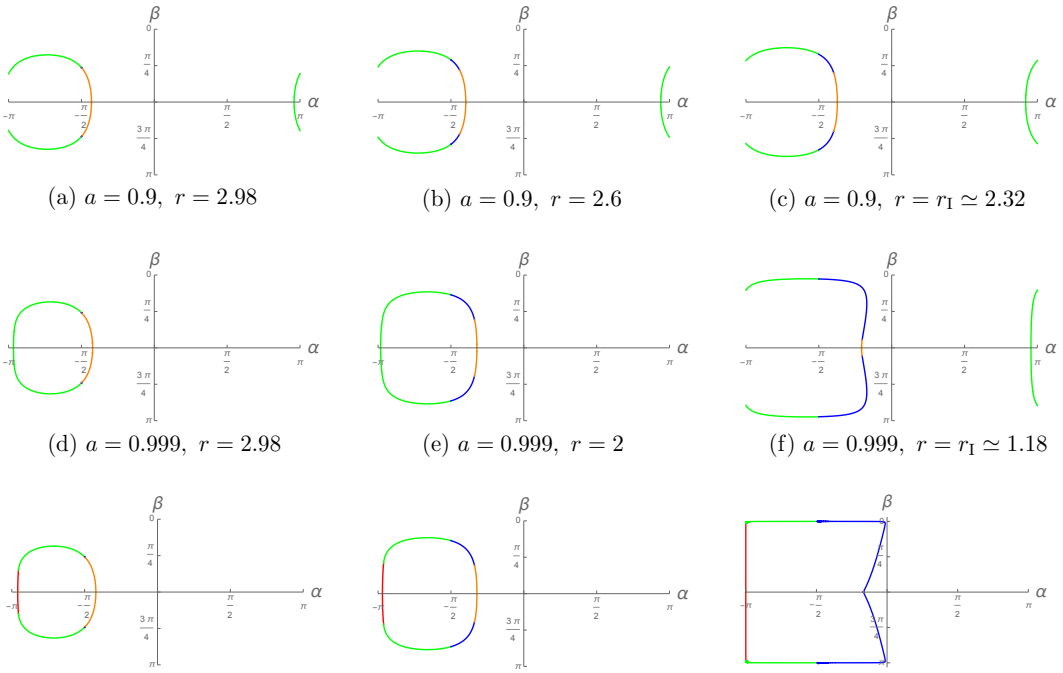

(a) $a = 0.9,\ r = 2.98$ (b) $a = 0.9,\ r = 2.6$ (c) $a = 0.9,\ r = r_{\rm I} \simeq 2.32$

(d) $a = 0.999,\ r = 2.98$ (e) $a = 0.999,\ r = 2$ (f) $a = 0.999,\ r = r_{\rm I} \simeq 1.18$

(g) $a = 1,\ r = 2.98$ (h) $a = 1,\ r = 2$ (i) $a = 1,\ r = 1.001$

Figure 4.4: Escape cone of a photon emitted at a source circularly orbiting a rotating black hole. The first, second, and third lines show the cases $a = 0.9$, $a = 0.999$, and $a = 1$, respectively. The red, green, blue, and orange lines show $(\alpha_{1(\rm a)}, \beta_{1(\rm a)})$, $(\alpha_{1(\rm b)}, \beta_{1(\rm b)})$, $(\alpha_{1(\rm c)}, \beta_{1(\rm c)})$, and (α_2, β_2), respectively. The area containing the origin bounded by the colored lines corresponds to the escape cone of a photon.

the last three terms coincide with each other,

$$\frac{{\rm d}\alpha_{1(\rm b)}}{{\rm d}r_1}\cos\beta_{1(\rm b)}\bigg|_{r_1=x} = \frac{{\rm d}\alpha_{1(\rm c)}}{{\rm d}r_1}\cos\beta_{1(\rm c)}\bigg|_{r_1=x} = \frac{{\rm d}\alpha_2}{{\rm d}r_2}\cos\beta_2\bigg|_{r_2=x} \equiv \tilde{g}(x). \tag{4.39}$$

Hence, we have

$$P = 1 - \frac{1}{2\pi}\int_{r_{\rm pc}^-}^{r_{\rm pc}^+} \tilde{g}(x){\rm d}x. \tag{4.40}$$

In the extremal case, we can also write P in terms of critical angles as follows:

$$P = 1 - \frac{1}{2\pi}\int_0^{r_{\rm h}} {\rm d}r_1 \frac{{\rm d}\alpha_{1(\rm a)}}{{\rm d}r_1}\cos\beta_{1(\rm a)} - \frac{1}{2\pi}\int_{r_{\rm h}}^{r_{\rm pc}^+} {\rm d}x\tilde{g}(x). \tag{4.41}$$

We note that the value of the escape probability in the subextremal case coincides with the one in the extremal case in the extremal limit: $a \to 1$. Since in the

subextremal case, the effective potentials b_1 and b_2 that are governing the photon escape in the radial direction approach those of the extremal case as a approaches 1, , the case (b) contains the equivalent effect of case (a) in the extremal limit. Furthermore, in the extremal limit, $r_{\rm pc}^-$ coincides with the horizon radius. Therefore, in the subextremal case, the escape probability coincides with that of the extremal case in the extremal limit.

Figure 4.5 shows the dependence of the escape probability P on the orbital radius r of a circularly orbiting source. The pink, gray, orange, blue, green, and red lines show the cases $a = 0.9, 0.95, 0.98, 0.999, 0.99999$, and 1, respectively. All P values decrease monotonically as r decreases toward $r_{\rm I}$. Furthermore, the value of P evaluated at $r = r_{\rm I}$ decreases monotonically as a approaches 1. For example, in the Thorne limit $a = 0.998$ [80], the value of P evaluated at the ISCO is

$$P(r_{\rm I}) = 0.5880\cdots , \tag{4.42}$$

where $r_{\rm I} = 1.236\cdots$. These results are consistent with a naive expectation that P becomes smaller as r approaches $r_{\rm h}$. However, it is worth noting that $P(r_{\rm I})$ does not approach zero as a approaches 1. Even if a photon is emitted from the source circularly orbiting a near-extremal Kerr black hole with the orbital radius $r = r_{\rm I} \simeq r_{\rm h}$, the escape probability is about 55%. For the extremal case, in the limit as r approaches $r_{\rm I}$ (i.e., the horizon radius $r_{\rm I} = r_{\rm h} = 1$), P takes a nonzero value [2],

$$\lim_{r\to 1^+} P = 0.5464\cdots . \tag{4.43}$$

This indicates that more than half of photons emitted in the vicinity of the horizon escape to infinity without falling into the central black hole. It is worth comparing these results with those obtained in [55]. The authors of [55] assumed a different situation from us for a light source: the right source is at rest with respect to a locally nonrotating observer, i.e., a non-angular momentum observer. In that

[2] The analytic expression of the escape probability at the ISCO in the extremal case have been obtained in [81]. The value is given by

$$P = \frac{5}{12} + \frac{\arctan\sqrt{5/3}}{\sqrt{5}\pi} = 0.5464\cdots .$$

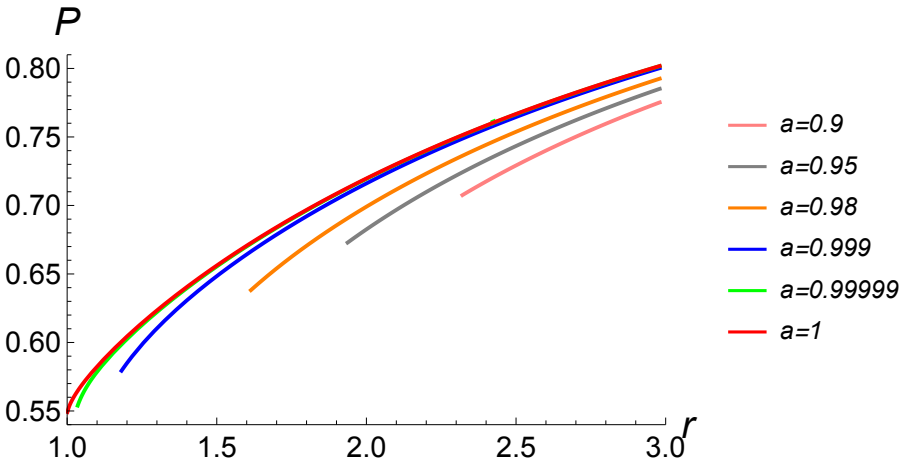

Figure 4.5: Dependence of the escape probability P on the orbital radius r of a circularly orbiting source. The pink, gray, orange, blue, green, and red lines correspond to the cases $a = 0.9, 0.95, 0.98, 0.999, 0.99999$, and 1, respectively. The left end point on each line corresponds to ISCO for subextremal cases, and the left end point for $a = 1$ is $r = 1.001$.

case, for the extremal Kerr black hole, the escape probability of a photon from a light source located at arbitrary close to the event horizon is 29.1%. This indicates that the escape probability is sensitive to the light source's motion. In particular, combining their result and our result that the photon escape probability from the ISCO in the extremal case is 54.6%, we can state the circularly orbiting light sources are more visible than the light source at rest with respect to the non-angular momentum observer.

We now evaluate the frequency shift of photons escaping from the ISCO to infinity. The redshift factor $\tilde{z}$ measured by a static observer at infinity is given by

$$1 + \tilde{z} = -k^{(0)}. \tag{4.44}$$

Figures 4.6(a)–4.6(c) show the density contour plots of $\tilde{z}$ for photons emitted from the front hemisphere of the source, which corresponds to the cases in Figs. 4.4(c), 4.4(f), and 4.4(i), respectively. The gray dashed lines show the contours of $\tilde{z} = 0$, and the red/blue regions show the emission angles with which a photon is redshifted/blueshifted. As a increases, the emission angles indicating blueshift

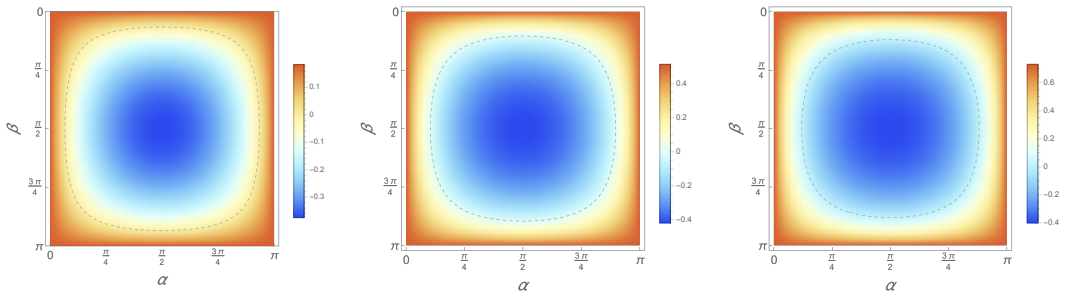

(a) $a = 0.9$, $r = r_{\rm I} = 2.320\cdots$ (b) $a = 0.999$, $r = r_{\rm I} = 1.181\cdots$ (c) $a = 1$, $r = 1.001$

Figure 4.6: Density contour plot of the redshift factor $\tilde{z}$ in the ranges $0 \leq \alpha \leq \pi$ and $0 \leq \beta \leq \pi$ (i.e., front side emission). The gray dashed lines indicate the contour $\tilde{z} = 0$. The red and blue regions denote redshift and blueshift, respectively.

decrease, but more than half of the hemisphere still shows blueshift.[3] This means that blueshifted photons reach to a observer at infinity, even if the orbital radius of the light source is sufficiently close to the horizon radius. Therefore, combined with the escape probability results, this implies that, in principle, photons escaping from the vicinity of the black hole horizon certainly transport the information of the near-horizon region and relativistic phenomena to distant observers.

[3]In the extremal Kerr geometry, it is known that $\tilde{z}$ varies smoothly with the directional cosine Ψ with respect to ϕ-direction, and there always exists the range of Ψ where $\tilde{z}$ shows a net blueshift [57].

Chapter 5

Conclusions and discussions

In this thesis, we have studied circular orbits of test particles around compact objects and its observability. In particular, we have discussed circular orbits of massive and massless particles in the Majumdar–Papapetrou dihole spacetime, and the escape probability of photons from the vicinity of the event horizon of a near-extremal Kerr black hole.

In chapter 2, we have reviewed circular orbits of particles around the Schwarzschild spacetime and the Kerr spacetime. Investigating circular orbits around a compact object is the most fundamental problem to know properties of the gravitational field generated by the compact object, and it is widely applicable from theoretical issues to observational issues. We have seen that the strong gravity field deflects a particle's orbit. In a black hole spacetime, there are some characteristic radii for particle motion, e.g, the circular photon orbit and the innermost stable circular orbit (ISCO). In the Kerr spacetime, the positions of such characteristic radii of circular orbits depend on the Kerr parameter defined as the magnitude of the angular momentum of the black hole divided by the black hole mass. We have seen that the radii of the circular photon orbit and the ISCO coincide with the horizon radius in the extremal limit.

In chapter 3, we have investigated the effect of a second compact object on the stable circular orbits using the Majumdar–Papapetrou dihole spacetime. The Majumdar–Papapetrou dihole spacetime is an exact solution of a two-parameter family in Einstein–Maxwell theory and consists of two extremal Reissner–Nordstöm black holes. In Majumdar–Papapetrou dihole spacetime, the positions of circular

orbits deviate from those of a single black hole case due to the second compact object. We have completely classified whole parameter ranges of the separation and the mass ratio according to the appearance of circular orbits. For the equal mass Majumdar–Papapetrou dihole spacetime, we have divided the parameter range of the separation d into five parts based on qualitative differences of the sequence of stable circular orbits and simultaneously have determined the four critical values as the boundaries of the parts: d_0, d_*, d_∞ and d_c. The inverses of two critical values d_* and d_∞ coincide with the critical values M_* and $\bar{M}$ mentioned in [41], respectively. The number of the marginally stable circular orbits increases due to the bifurcation or the separation of the sequence. The ISCO radius can be smaller than that in the single extremal Reissner–Nordström black hole spacetime. The location of the ISCO changes discontinuously at $d = d_\mathrm{c}$. For the different mass Majumdar–Papapetrou dihole spacetime, while the parameter range of the separation of the two objects is divided due to the appearance of stable circular orbits, this division depends on its mass ratio. We have shown that the mass ratio range separates into four parts and found three critical values as the boundaries: ν_∞, ν_*, and ν_0. In the context of the quasinormal mode, the frequency is known to correspond to the orbital frequency of the unstable circular photon orbit. Since our results show that the orbital frequency can be comparable to that of a circular massive particle orbit, we can expect that the resonant excitation of the quasinormal mode that is characteristic mode of the dihole spacetime occurs [82].

We should discuss a possible implication for a more realistic binary black hole system. The Majumdar–Papapetrou dihole spacetime we have used in the background is static, but a realistic binary system is a dynamic system. This fact does not imply that our analysis is meaningless. Let us consider an example. For simplicity, here, we assume that two black holes are equal mass, the second black hole takes the Kepler motion with the zero eccentricity around a main black hole, and a test particle circularly orbits a main black hole on the ISCO. In the present case, the orbital periods for both the second black hole T_b and the test particle T_I are determined by the Kepler orbital period. The orbital period is proportional to $r^{3/2}$, where r is the distance between the main black hole and an orbiter. Applying values of the ISCOs in the MP dihole spacetime, the value of the separation parameter is $d \geq 6.33 \sim 31.8$ for the orbital period of a test particle to become more than $10 \sim 100$ times that of the binary black hole: $T_\mathrm{b}/T_\mathrm{I} \geq 10 \sim 100$. Therefore,

the classifications of circular orbits in the Majumdar–Papapetrou dihole spacetime with $d \geq 6.33 \sim 31.8$ may be a criterion for investigating the initial conditions for phenomena occurring around a slowly evolving binary black hole. If we focus on circular photon orbits, we may extend the validity range of the separation parameter. Though it is interesting to take into account the dynamic features, we will analyze this topic in future work.

In chapter 4, we have analyzed the escape probability of photons from a circularly orbiting light source in a near-extremal Kerr black hole to discuss the observability of the near-horizon region. Because, in particular, the ISCO radius is very close to the horizon radius in a near-extremal Kerr spacetime, the escape probability of a photon from the ISCO indicates the observability of the near-horizon region. The observability is essential for distinguishing whether or not the central object is a black hole. We have shown that the escape probability evaluated at the ISCO decreases monotonically when the Kerr parameter approaches the extremal value. Despite the fact that the ISCO radius eventually coincides with the horizon radius in the extremal case [65, 66], the probability take a nonzero value 54.6% even in the limit of the ISCO. This value is larger than the escape probability 29.1% for the case where assumes the light source at rest with respect to the locally nonrotating observer. We have also found that photons emitted from the front side of the source get blueshifted for distant observers even if the emission point is sufficiently close to the ISCO in the extremal Kerr black hole. From these results, we conclude that, in principle, the near-horizon region of a rapidly rotating black hole is observable.

Our results provide insight into optical phenomena such as the observation of a black hole shadow. The ISCO is often identified as the innermost edge of the accretion disk or is considered as the position where the phase of accretion flow switches. However, in any case, the orbit is located in the immediate vicinity of the near-extremal rotating black hole. Photons emitted from this region contain information on the near-horizon region and phenomena and certainly transport it to infinity. Finally, the information can be obtained from photons that appear as the edge of the black hole shadow to a distant observer. From this, if a black hole is rapidly spinning, in principle, signs of near-horizon physics will be detectable on the edge of the shadow.

Appendix A

Circular photon orbits in the equal mass Majumdar–Papapetrou dihole spacetime

We review circular photon orbits in the MP dihole spacetime with equal unit mass $M_\pm = 1$. The effective potential for null particles is given by Eq. (3.9) with $\kappa = 0$. As is the case with timelike particles, the condition $V_z = 0$ is equivalent to $U_z = 0$ and has solutions $\rho = \rho_0$ and $z = 0$. We focus on circular photon orbits on $\rho = \rho_0$. To investigate their positions, we solve Eq. (3.27) again for z and find real roots $z_0(\rho)$. The line $z = z_0$ corresponds to the line $\rho = \rho_0$. We consider the condition $V_\rho = 0$ on $z = z_0$:

$$V_\rho(\rho, z_0(\rho)) = 0. \tag{A.1}$$

The real solutions of this equation express the radii of the unstable circular photon orbits. They only exist for $d \geq d_\mathrm{c}$ but not for $d < d_\mathrm{c}$. The dependence of the radii of circular photon orbits on the separation parameter d is shown in Fig. 3.2 by orange dashed lines. In the limit as $d \to \infty$, the circular photon orbit radius measured by ρ approaches 1, which coincides with that of the single Reissner–Nordström black hole spacetime.

Next we focus on circular photon orbits on $z = 0$ plane. The condition $V_\rho = 0$

leads to

$$\left(\rho^2 + d^2\right)^{3/2} = 2\left(\rho^2 - d^2\right). \tag{A.2}$$

This equation has real roots only for $\rho > d$. We can rewrite Eq. (A.2)

$$F = 0, \tag{A.3}$$

where F is defined by Eq. (3.32). In the range $\rho > d$, the roots of this cubic equation for ρ^2 are given by

$$\rho_{\rm pu}^2 = \frac{4 - 3d^2}{3} + \frac{8}{3}\sqrt{1 - 3d^2}\cos\left[\frac{1}{3}\arccos\frac{27d^4 - 36d^2 + 8}{8\left(1 - 3d^2\right)^{3/2}}\right], \tag{A.4}$$

$$\rho_{\rm ps}^2 = \frac{4 - 3d^2}{3} + \frac{8}{3}\sqrt{1 - 3d^2}\cos\left[\frac{4\pi}{3} + \frac{1}{3}\arccos\frac{27d^4 - 36d^2 + 8}{8\left(1 - 3d^2\right)^{3/2}}\right]. \tag{A.5}$$

Note that $\rho_{\rm pu}$ and $\rho_{\rm ps}$ correspond to the unstable circular photon orbit and the stable one, respectively (see Fig. 3.2). These roots are real only for $d \leq d_\infty$, which is found from the discriminant of Eq. (A.3). Hence, for $d > d_\infty$, there exist unstable circular photon orbits only on $\rho = \rho_0$ line [see Figs. 3.1(a)–3.1(e)]. When $d = d_\infty$, an additional circular photon orbit appears at $(\rho, z) = (\rho_\infty, 0)$ [see Fig. 3.1(f)], where ρ_∞ is given by Eq. (3.47). The condition for the existence of the multiple root $\rho_{\rm pu} = \rho_{\rm ps}$ also leads to the values of d_∞ and ρ_∞. For $d_{\rm c} < d < d_\infty$, unstable circular photon orbits exist on $\rho = \rho_0$ and at $(\rho, z) = (\rho_{\rm pu}, 0)$, and stable circular photon orbits exists at $(\rho, z) = (\rho_{\rm ps}, 0)$ [see Fig. 3.1(g)]. When $d = d_{\rm c}$, three circular photon orbits degenerate at $(\rho, z) = (\sqrt{2}d_{\rm c}, 0)$ [see Fig. 3.1(h)]. For $d < d_{\rm c}$, there is no stable circular photon orbit but there are two unstable circular photon orbits on $z = 0$. The outer one is radially unstable but vertically stable, while the inner one is radially stable but vertically unstable (see also Ref. [40]). For $d = 0$, we obtain $\rho_{\rm pu} = 2$ and $\rho_{\rm ps} = 0$, which coincide with the radius of the unstable circular photon orbit and the horizon radius of the single extremal Reissner–Nordström black hole with mass 2, respectively.

Bibliography

[1] A. Einstein, *The Field Equations of Gravitation*, Sitzungsber. Preuss. Akad. Wiss. Berlin (Math. Phys.) **1915** (1915) 844–847.

[2] A. Einstein, *The Foundation of the General Theory of Relativity*, Annalen Phys. **49** (1916), no. 7 769–822.

[3] C. M. Will, Theory and Experiment in Gravitational Physics. Cambridge University Press, 1993.

[4] K. Schwarzschild, *On the gravitational field of a sphere of incompressible fluid according to Einstein's theory*, Sitzungsber. Preuss. Akad. Wiss. Berlin (Math. Phys.) **1916** (1916) 424–434 [physics/9912033].

[5] R. P. Kerr, *Gravitational field of a spinning mass as an example of algebraically special metrics*, Phys. Rev. Lett. **11** (1963) 237–238.

[6] **LIGO Scientific, Virgo** Collaboration, B. Abbott et. al., *Observation of Gravitational Waves from a Binary Black Hole Merger*, Phys. Rev. Lett. **116** (2016), no. 6 061102 [1602.03837].

[7] **Event Horizon Telescope** Collaboration, K. Akiyama et. al., *First M87 Event Horizon Telescope Results. I. The Shadow of the Supermassive Black Hole*, Astrophys. J. **875** (2019), no. 1 L1 [1906.11238].

[8] **Event Horizon Telescope** Collaboration, K. Akiyama et. al., *First M87 Event Horizon Telescope Results. II. Array and Instrumentation*, Astrophys. J. Lett. **875** (2019), no. 1 L2 [1906.11239].

[9] **Event Horizon Telescope** Collaboration, K. Akiyama et. al., *First M87 Event Horizon Telescope Results. III. Data Processing and Calibration*, Astrophys. J. Lett. **875** (2019), no. 1 L3 [1906.11240].

[10] **Event Horizon Telescope** Collaboration, K. Akiyama et. al., *First M87 Event Horizon Telescope Results. IV. Imaging the Central Supermassive Black Hole*, Astrophys. J. Lett. **875** (2019), no. 1 L4 [1906.11241].

[11] **Event Horizon Telescope** Collaboration, K. Akiyama et. al., *First M87 Event Horizon Telescope Results. V. Physical Origin of the Asymmetric Ring*, Astrophys. J. Lett. **875** (2019), no. 1 L5 [1906.11242].

[12] **Event Horizon Telescope** Collaboration, K. Akiyama et. al., *First M87 Event Horizon Telescope Results. VI. The Shadow and Mass of the Central Black Hole*, Astrophys. J. Lett. **875** (2019), no. 1 L6 [1906.11243].

[13] **GRAVITY** Collaboration, R. Abuter et. al., *Detection of the gravitational redshift in the orbit of the star S2 near the Galactic centre massive black hole*, Astron. Astrophys. **615** (2018) L15 [1807.09409].

[14] T. Do et. al., *Relativistic redshift of the star S0-2 orbiting the Galactic center supermassive black hole*, Science **365** (2019), no. 6454 664–668 [1907.10731].

[15] H. Saida et. al., *A significant feature in the general relativistic time evolution of the redshift of photons coming from a star orbiting Sgr A**, Publ. Astron. Soc. Jap. **71** (2019), no. 6 126 [1910.02632].

[16] **GRAVITY** Collaboration, R. Abuter et. al., *Detection of the Schwarzschild precession in the orbit of the star S2 near the Galactic centre massive black hole*, Astron. Astrophys. **636** (2020) L5 [2004.07187].

[17] I. Novikov and K. Thorne, *Astrophysics and black holes*, in Les Houches Summer School of Theoretical Physics: Black Holes, pp. 343–550, 1973.

[18] J. P. A. Clark and D. M. Eardley, *Evolution of close neutron star binaries.*, Astrophys. J. **215** (July, 1977) 311–322.

[19] L. E. Kidder, C. M. Will and A. G. Wiseman, *Coalescing binary systems of compact objects to (post)**(5/2)-Newtonian order. 3. Transition from inspiral to plunge*, Phys. Rev. D **47** (1993) 3281–3291.

[20] **LIGO Scientific, Virgo** Collaboration, B. Abbott et. al., *GWTC-1: A Gravitational-Wave Transient Catalog of Compact Binary Mergers Observed by LIGO and Virgo during the First and Second Observing Runs*, Phys. Rev. X **9** (2019), no. 3 031040 [1811.12907].

[21] **LIGO Scientific, Virgo** Collaboration, R. Abbott et. al., *GWTC-2: Compact Binary Coalescences Observed by LIGO and Virgo During the First Half of the Third Observing Run*, 2010.14527.

[22] K. Yamada and H. Asada, *Collinear solution to the general relativistic three-body problem*, Phys. Rev. D **82** (2010) 104019 [1010.2284].

[23] K. Yamada and T. Tsuchiya, *The linear stability of the post-Newtonian triangular equilibrium in the three-body problem*, 1612.08361.

[24] N. Seto, *Relativistic Resonant Relations between Massive Black Hole Binary and Extreme Mass Ratio Inspiral*, Phys. Rev. D **85** (2012) 064037 [1202.4761].

[25] P. Gupta, H. Suzuki, H. Okawa and K.-i. Maeda, *Gravitational Waves from Hierarchical Triple Systems with Kozai-Lidov Oscillation*, Phys. Rev. D **101** (2020), no. 10 104053 [1911.11318].

[26] H. Suzuki, P. Gupta, H. Okawa and K.-i. Maeda, *Cumulative shift of periastron time of binary pulsar with Kozai–Lidov oscillation*, Mon. Not. Roy. Astron. Soc. **486** (2019), no. 1 L52–L57 [1903.00287].

[27] L. Wen, *On the eccentricity distribution of coalescing black hole binaries driven by the Kozai mechanism in globular clusters*, Astrophys. J. **598** (2003) 419–430 [astro-ph/0211492].

[28] N. Seto, *Highly Eccentric Kozai Mechanism and Gravitational-Wave Observation for Neutron Star Binaries*, Phys. Rev. Lett. **111** (2013) 061106 [1304.5151].

[29] Y. Meiron, B. Kocsis and A. Loeb, *Detecting triple systems with gravitational wave observations*, Astrophys. J. **834** (2017), no. 2 200 [1604.02148].

[30] A. Bohn, W. Throwe, F. Hébert, K. Henriksson, D. Bunandar, M. A. Scheel and N. W. Taylor, *What does a binary black hole merger look like?*, Class. Quant. Grav. **32** (2015), no. 6 065002 [1410.7775].

[31] H. Weyl, *The theory of gravitation*, Annalen Phys. **54** (1917) 117–145.

[32] S. Majumdar, *A class of exact solutions of Einstein's field equations*, Phys. Rev. **72** (1947) 390–398.

[33] A. Papaetrou, *A Static solution of the equations of the gravitational field for an arbitrary charge distribution*, Proc. Roy. Irish Acad. A **A51** (1947) 191–204.

[34] J. Hartle and S. Hawking, *Solutions of the Einstein-Maxwell equations with many black holes*, Commun. Math. Phys. **26** (1972) 87–101.

[35] D. Kramer and G. Neugebauer, *The superposition of two Kerr solutions*, Physics Letters A **75** (Jan., 1980) 259–261.

[36] D. Nitta, T. Chiba and N. Sugiyama, *Shadows of Colliding Black Holes*, Phys. Rev. D **84** (2011) 063008 [1106.2425].

[37] M. Patil, P. Mishra and D. Narasimha, *Curious case of gravitational lensing by binary black holes: a tale of two photon spheres, new relativistic images and caustics*, Phys. Rev. D **95** (2017), no. 2 024026 [1610.04863].

[38] T. Assumpcao, V. Cardoso, A. Ishibashi, M. Richartz and M. Zilhao, *Black hole binaries: ergoregions, photon surfaces, wave scattering, and quasinormal modes*, Phys. Rev. D **98** (2018), no. 6 064036 [1806.07909].

[39] P. V. Cunha, C. A. Herdeiro and M. J. Rodriguez, *Shadows of Exact Binary Black Holes*, Phys. Rev. D **98** (2018), no. 4 044053 [1805.03798].

[40] J. Shipley and S. R. Dolan, *Binary black hole shadows, chaotic scattering and the Cantor set*, Class. Quant. Grav. **33** (2016), no. 17 175001 [1603.04469].

[41] A. Wunsch, T. Müller, D. Weiskopf and G. Wunner, *Circular orbits in the extreme Reissner-Nordstrøm dihole metric*, Phys. Rev. D **87** (2013), no. 2 024007 [1301.7560].

[42] S. R. Dolan and J. O. Shipley, *Stable photon orbits in stationary axisymmetric electrovacuum spacetimes*, Phys. Rev. D **94** (2016), no. 4 044038 [1605.07193].

[43] K. Nakashi and T. Igata, *Innermost stable circular orbits in the Majumdar-Papapetrou dihole spacetime*, Phys. Rev. D **99** (2019), no. 12 124033 [1903.10121].

[44] K. Nakashi and T. Igata, *Effect of a second compact object on stable circular orbits*, Phys. Rev. D **100** (2019), no. 10 104006 [1908.10075].

[45] K. Gebhardt, J. Adams, D. Richstone, T. R. Lauer, S. M. Faber, K. Gültekin, J. Murphy and S. Tremaine, *THE BLACK HOLE MASS IN M87 FROM GEMINI/NIFS ADAPTIVE OPTICS OBSERVATIONS*, The Astrophysical Journal **729** (Feb, 2011) 119.

[46] J. L. Walsh, A. J. Barth, L. C. Ho and M. Sarzi, *THE M87 BLACK HOLE MASS FROM GAS-DYNAMICAL MODELS OF SPACE TELESCOPE IMAGING SPECTROGRAPH OBSERVATIONS*, The Astrophysical Journal **770** (May, 2013) 86.

[47] Y. Mizuno, Z. Younsi, C. M. Fromm, O. Porth, M. De Laurentis, H. Olivares, H. Falcke, M. Kramer and L. Rezzolla, *The Current Ability to Test Theories of Gravity with Black Hole Shadows*, Nature Astron. **2** (2018), no. 7 585–590 [1804.05812].

[48] V. Cardoso and P. Pani, *Testing the nature of dark compact objects: a status report*, Living Rev. Rel. **22** (2019), no. 1 4 [1904.05363].

[49] S. S. Doeleman et. al., *Jet Launching Structure Resolved Near the Supermassive Black Hole in M87*, Science **338** (2012) 355 [1210.6132].

[50] Y.-R. Li, Y.-F. Yuan, J.-M. Wang, J.-C. Wang and S. Zhang, *Constraining spins of supermassive black holes from TeV variability. II. fully general relativistic calculations*, Astrophys. J. **699** (2009) 513 [0904.2335].

[51] J. Feng and Q. Wu, *Constraint on the black-hole spin of M87 from the accretion-jet model*, Mon. Not. Roy. Astron. Soc. **470** (2017) 612 [1705.07804].

[52] A. Lupsasca, A. P. Porfyriadis and Y. Shi, *Critical Emission from a High-Spin Black Hole*, Phys. Rev. D **97** (2018), no. 6 064017 [1712.10182].

[53] T. Igata, H. Ishihara and Y. Yasunishi, *Observability of spherical photon orbits in near-extremal Kerr black holes*, Phys. Rev. D **100** (2019), no. 4 044058 [1904.00271].

[54] K. Ogasawara, T. Harada, U. Miyamoto, T. Igata and M. Patil, *Escape probability of the super-Penrose process*, Phys. Rev. D **95** (2017), no. 12 124019 [1609.03022].

[55] K. Ogasawara, T. Igata, T. Harada and U. Miyamoto, *Escape probability of a photon emitted near the black hole horizon*, Phys. Rev. D **101** (2020), no. 4 044023 [1910.01528].

[56] R. Takahashi and M. Takahashi, *Anisotropic radiation field and trapped photons around the Kerr black hole*, Astron. Astrophys. **513** (2010) A77 [1002.4245].

[57] C. T. Cunningham and J. M. Bardeen, *The Optical Appearance of a Star Orbiting an Extreme Kerr Black Hole*, Astrophys. J. **183** (July, 1973) 237–264.

[58] C. Cunningham, *The effects of redshifts and focusing on the spectrum of an accretion disk around a Kerr black hole*, Astrophys. J. **202** (1975) 788–802.

[59] J.-P. Luminet, *Image of a spherical black hole with thin accretion disk*, Astron. Astrophys. **75** (1979) 228–235.

[60] J. Fukue and T. Yokoyama, *Color photographs of an accretion disk around a black hole*, Publ. Astron. Soc. Jpn. **40** (Jan., 1988) 15–24.

[61] H. Falcke, F. Melia and E. Agol, *Viewing the shadow of the black hole at the galactic center*, Astrophys. J. Lett. **528** (2000) L13 [astro-ph/9912263].

[62] R. Takahashi, *Shapes and positions of black hole shadows in accretion disks and spin parameters of black holes*, J. Korean Phys. Soc. **45** (2004) S1808–S1812 [astro-ph/0405099].

[63] T. Kawashima, M. Kino and K. Akiyama, *Black Hole Spin Signature in the Black Hole Shadow of M87 in the Flaring State*, Astrophys. J. **878** (2019), no. 1 27 [1905.10717].

[64] S. E. Gralla and A. Lupsasca, *Lensing by Kerr Black Holes*, Phys. Rev. D **101** (2020), no. 4 044031 [1910.12873].

[65] J. M. Bardeen, W. H. Press and S. A. Teukolsky, *Rotating black holes: Locally nonrotating frames, energy extraction, and scalar synchrotron radiation*, Astrophys. J. **178** (1972) 347.

[66] D. Kapec and A. Lupsasca, *Particle motion near high-spin black holes*, Class. Quant. Grav. **37** (2020), no. 1 015006 [1905.11406].

[67] T. Igata, K. Nakashi and K. Ogasawara, *Observability of the innermost stable circular orbit in a near-extremal Kerr black hole*, Phys. Rev. D **101** (2020), no. 4 044044 [1910.12682].

[68] M. Heusler, Black Hole Uniqueness Theorems. Cambridge Lecture Notes in Physics. Cambridge University Press, 1996.

[69] R. Wald, General Relativity. University of Chicago Press, 1984.

[70] C. A. Herdeiro and J. M. Oliveira, *On the inexistence of solitons in Einstein–Maxwell-scalar models*, Class. Quant. Grav. **36** (2019), no. 10 105015 [1902.07721].

[71] B. Carter, *Killing horizons and orthogonally transitive groups in space-time*, J. Math. Phys. **10** (1969) 70–81.

[72] K. Nakashi and M. Kimura, *Towards rotating non-circular black holes in string-inspired gravity*, 2008.04003.

[73] B. Carter, *Global structure of the Kerr family of gravitational fields*, Phys. Rev. **174** (1968) 1559–1571.

[74] M. Walker and R. Penrose, *On quadratic first integrals of the geodesic equations for type [22] spacetimes*, Commun. Math. Phys. **18** (1970) 265–274.

[75] E. Teo, *Spherical Photon Orbits Around a Kerr Black Hole*, General Relativity and Gravitation **35** (Nov., 2003) 1909–1926.

[76] V. Cardoso, A. S. Miranda, E. Berti, H. Witek and V. T. Zanchin, *Geodesic stability, Lyapunov exponents and quasinormal modes*, Phys. Rev. D **79** (2009) 064016 [0812.1806].

[77] T. Igata, H. Ishihara and Y. Takamori, *Stable Bound Orbits around Black Rings*, Phys. Rev. D **82** (2010) 101501 [1006.3129].

[78] T. Igata, H. Ishihara and H. Yoshino, *Integrability of Particle System around a Ring Source as the Newtonian Limit of a Black Ring*, Phys. Rev. D **91** (2015), no. 8 084042 [1412.7033].

[79] S. Chandrasekhar, The mathematical theory of black holes. Oxford classic texts in the physical sciences. Oxford Univ. Press, Oxford, 2002.

[80] K. S. Thorne, *Disk accretion onto a black hole. 2. Evolution of the hole.*, Astrophys. J. **191** (1974) 507–520.

[81] D. E. Gates, S. Hadar and A. Lupsasca, *Photon Emission from Circular Equatorial Kerr Orbiters*, 2010.07330.

[82] L. Bernard, V. Cardoso, T. Ikeda and M. Zilhão, *Physics of black hole binaries: Geodesics, relaxation modes, and energy extraction*, Phys. Rev. D **100** (2019), no. 4 044002 [1905.05204].